

From “The Cliff” to “Virgil”: Mapping the Spectral Diversity of Little Red Dots with JWST/NIRSpec

GUILLERMO BARRO ¹, PABLO G. PÉREZ-GONZÁLEZ ², DALE KOCEVSKI ³, JONATHAN R. TRUMP ⁴,
MARK DICKINSON ⁵, PABLO ARRABAL HARO ^{6,7}, MADISYN BROOKS ⁴, CALLUM T. DONNAN ⁵,
JAMES S. DUNLOP ⁸, STEVEN L. FINKELSTEIN ^{9,10}, MAXIMILIEN FRANCO ¹¹, GIOVANNI GANDOLFI ¹²,
MAURO GIAVALISCO ¹³, NORMAN A. GROGIN ¹⁴, MICHAELA HIRSCHMANN ¹⁵, JEYHAN S. KARTALTEPE ¹⁶,
ANTON M. KOEKEMOER ¹⁴, REBECCA L. LARSON ^{14,*}, GENE C. K. LEUNG ¹⁷, RAY A. LUCAS ¹⁴,
ELIZABETH J. MCGRATH ³, CASEY PAPOVICH ^{18,19}, BORJA PÉREZ-DÍAZ ¹², RACHEL S. SOMERVILLE ²⁰,
ELIZABETH TAYLOR ²¹, ANTHONY J. TAYLOR ^{9,10}, ROBERTA TRIPODI ¹², L. Y. AARON YUNG ^{22,*} AND
XIN WANG ^{23,24,25}

¹University of the Pacific, Stockton, CA 90340 USA

²Centro de Astrobiología (CAB), CSIC-INTA, Ctra. de Ajalvir km 4, Torrejón de Ardoz, E-28850, Madrid, Spain

³Department of Physics and Astronomy, Colby College, Waterville, ME 04901, USA

⁴Department of Physics, 196A Auditorium Road, Unit 3046, University of Connecticut, Storrs, CT 06269, USA

⁵NSF National Optical-Infrared Astronomy Research Laboratory, 950 N. Cherry Ave., Tucson, AZ 85719, USA

⁶Center for Space Sciences and Technology, UMBC, 5523 Research Park Dr, Baltimore, MD 21228 USA

⁷Astrophysics Science Division, NASA Goddard Space Flight Center, 8800 Greenbelt Rd, Greenbelt, MD 20771, USA

⁸Institute for Astronomy, University of Edinburgh, Royal Observatory, Edinburgh, EH9 3HJ, UK

⁹Department of Astronomy, The University of Texas at Austin, Austin, TX, USA

¹⁰Cosmic Frontier Center, The University of Texas at Austin, Austin, TX, USA

¹¹Université Paris-Saclay, Université Paris Cité, CEA, CNRS, AIM, 91191 Gif-sur-Yvette, France

¹²INAF – Osservatorio Astronomico di Roma, via Frascati 33, 00078, Monteporzio Catone, Italy

¹³University of Massachusetts Amherst, 710 North Pleasant Street, Amherst, MA 01003-9305, USA

¹⁴Space Telescope Science Institute, 3700 San Martin Drive, Baltimore, MD 21218, USA

¹⁵Institute of Physics, Laboratory of Galaxy Evolution, Ecole Polytechnique Federale de Lausanne (EPFL), Observatoire de Sauverny, 1290 Versoix, Switzerland

¹⁶Laboratory for Multiwavelength Astrophysics, School of Physics and Astronomy, Rochester Institute of Technology, 84 Lomb Memorial Drive, Rochester, NY 14623, USA

¹⁷MIT Kavli Institute for Astrophysics and Space Research, 77 Massachusetts Ave., Cambridge, MA 02139, USA

¹⁸Department of Physics and Astronomy, Texas A&M University, College Station, TX, 77843-4242 USA

¹⁹George P. and Cynthia Woods Mitchell Institute for Fundamental Physics and Astronomy, Texas A&M University, College Station, TX, 77843-4242 USA

²⁰Center for Computational Astrophysics, Flatiron Institute, 162 5th Avenue, New York, NY 10010, USA

²¹Institute for Astronomy, University of Edinburgh, Royal Observatory, Edinburgh EH9 3HJ, UK

²²Space Telescope Science Institute, 3700 San Martin Dr., Baltimore, MD 21218, USA

²³School of Astronomy and Space Science, University of Chinese Academy of Sciences (UCAS), Beijing 100049, China

²⁴National Astronomical Observatories, Chinese Academy of Sciences, Beijing 100101, China

²⁵Institute for Frontiers in Astronomy and Astrophysics, Beijing Normal University, Beijing 102206, China

ABSTRACT

One of JWST’s most unexpected discoveries is the emergence of “Little Red Dots” (LRDs): compact sources at $z \gtrsim 3$ with blue rest-frame UV continua, red optical slopes, and broad Balmer emission lines that challenge standard models and suggest a population of early, unusual active galactic nuclei (AGNs). Using a comprehensive photometric selection and public NIRSpec/PRISM spectroscopy across six JWST deep fields, we identify a large sample of 118 LRDs with high-S/N spectra, enabling a population-wide analysis of their UV–optical continuum and emission lines. We find clear correlations between rest-frame UV–optical color ($[0.3\text{--}0.9 \mu\text{m}]$) and slopes: bluer LRDs have blue UV slopes ($\beta_{\nu,\text{UV}} \sim 0.3$) and red optical slopes, while redder LRDs exhibit redder UV slopes ($\beta_{\nu,\text{UV}} \sim 1.1$). The continuum shape shows a similar trend: redder LRDs display prominent Balmer breaks and curvature, while bluer LRDs follow power-law–like optical SEDs. From literature compilations, $\sim 60\%$ of known

broad-line AGNs satisfy our LRD criteria, and up to 90% of LRDs show broad Balmer lines. Emission-line diagnostics reveal a shift from high $H\alpha/H\beta$ and low $[\text{OIII}]\lambda 5007/H\beta$ in redder LRDs to the opposite in bluer ones, along with stronger narrow-line equivalent widths, suggesting a transition from AGN- to host-dominated emission. We fit the spectra with a two-component model combining a gas-shrouded black hole (BH) and a galaxy host. Redder LRDs require higher-luminosity, unreddened BHs and modestly reddened hosts; bluer LRDs require lower-luminosity, reddened BHs and dust-free galaxies. This framework reproduces the diversity in colors and spectral shape by varying BH luminosity, obscuration, and BH-to-host luminosity ratio.

Keywords: galaxies: spectroscopy — galaxies: high-redshift

1. INTRODUCTION

One of the most surprising and actively debated discoveries from the first years of JWST observations is the emergence of a populous class of compact, red sources at $z > 4$, now widely known as Little Red Dots (LRDs). These objects exhibit: (1) remarkably small, point-like morphologies; (2) unusual spectral energy distributions (SEDs) combining blue rest-frame ultraviolet (UV) continua with red rest-frame optical colors; and (3) a high incidence of broad permitted emission lines, with FWHM values of 2000–4000 km s^{-1} (Labbé et al. 2023; Barro et al. 2024a; Greene et al. 2024; Akins et al. 2024a; Kokorev et al. 2024a; Kocevski et al. 2024; Pérez-González et al. 2023a; Taylor et al. 2024).

Early interpretations of these properties suggest they could be dusty, compact, massive starburst galaxies (Labbé et al. 2023; Baggen et al. 2023; Pérez-González et al. 2023b; Barro et al. 2024a), faint, obscured active galactic nuclei (AGNs) (Kocevski et al. 2023a; Greene et al. 2024; Labbe et al. 2023), or a combination of both (Killi et al. 2023; Wang et al. 2024a; Barro et al. 2024a; Pérez-González et al. 2024; Leung et al. 2024). Despite the growing body of photometric and spectroscopic data, the physical nature of LRDs remains unresolved, as their properties differ significantly from those of typical high-redshift galaxies or AGNs, and are subject to strong modeling degeneracies that make interpretation difficult.

From the photometric perspective, large-area JWST surveys now routinely identify hundreds of LRDs across multiple deep fields using single- or multi-color selections designed to capture their distinctive “V-shaped” SEDs over a wide redshift range (Kokorev et al. 2024a; Kocevski et al. 2024; Akins et al. 2024a; Barro et al. 2024a). However, the inferred surface densities span a wide range, from ~ 0.25 to 1 arcmin^{-2} , depending on the adopted color thresholds, and increase system-

atically from the reddest to the bluest selections (e.g., $F277W-F444W > 1.5$ versus $F200W-F444W > 1$; Akins et al. 2024a; Barro et al. 2024b). This dependence on selection criteria indicates that LRDs constitute a far more diverse population than initially recognized, extending beyond the most extreme red objects and spanning a broad range of rest-frame UV-to-NIR colors of up to four magnitudes (Pérez-González et al. 2024; Barro et al. 2024b).

Mid- and far-infrared photometry has played a key role in constraining the dust content and emission properties of LRDs, placing important limits on both star-forming and AGN-driven models. The lack of detections in individual ALMA observations and deep submillimeter stacks suggests that LRDs do not exhibit the high infrared luminosities typical of dusty star-forming galaxies (Labbe et al. 2023; Akins et al. 2024a; Casey et al. 2024). If LRDs are dusty starbursts, their IR emission must arise from extremely compact, hot regions with unusually short-wavelength dust peaks (Pérez-González et al. 2023b, 2024). Conversely, near-to-mid IR colors from MIRI observations (Williams et al. 2024; Pérez-González et al. 2024; Akins et al. 2024a) are inconsistent with the warm dust torus emission expected from classical obscured AGNs. If LRDs are AGNs, they may instead host hot-dust-deficient tori (e.g., Lyu et al. 2017), with emission peaking at much longer wavelengths ($\sim 10\text{--}100 \mu\text{m}$) that remain largely inaccessible to current infrared facilities (Casey et al. 2024; Leung et al. 2024; Barro et al. 2024a).

On the spectroscopic front, JWST/NIRSpec MSA (Ferruit et al. 2022) has delivered over 200 spectra of LRDs, revealing emission lines in nearly all cases and firmly establishing the widespread presence of broad-line emission across the population (Greene et al. 2024; Kocevski et al. 2024; Taylor et al. 2024; Juodžbalis et al. 2025; Hviding et al. 2025). Just as critical, continuum detections have significantly shaped physical interpretations of LRDs. Initial reports of Balmer breaks in several sources pointed to stellar-dominated continua (Wang

* Giacconi Postdoctoral Fellow

et al. 2024a,b; Labbe et al. 2024). However, further observations revealed larger breaks increasingly inconsistent with stellar populations (Labbe et al. 2024; Ma et al. 2025; Ji et al. 2025), culminating in extreme cases with break strengths above 5 magnitudes (de Graaff et al. 2025a; Naidu et al. 2025; Taylor et al. 2025) that challenged the stellar origin.

This has led to alternative AGN models that invoke dense gas envelopes around accreting black holes similar to “quasi-stars” (Begelman & Dexter 2025) or “black hole stars” (Inayoshi & Maiolino 2024; Ji et al. 2025) that can naturally produce Balmer breaks as strong or stronger than those of evolved stars. These dense gas cocoons may also account for the narrow absorption features seen in some broad Balmer lines (Matthee et al. 2024; Kocevski et al. 2024; D’Eugenio et al. 2025a; Torralba et al. 2025), and their intrinsically red optical continua reduce the need for high dust reddening, easing tensions with mid- and far-infrared constraints. These advantages make variations of the dense-gas scenario a promising framework for explaining the nature of LRDs.

Still, while dense gas envelopes appear important in some LRDs, they do not yet offer a population-wide explanation. Can this model account for the full range of observed colors? What about LRDs without strong Balmer breaks or absorption features? Answering these questions requires determining what fraction of the population exhibits these traits. However, most current studies rely on small or heterogeneous samples, often based on photometric selections without spectroscopic confirmation or spectroscopic datasets that do not consistently apply photometric LRD criteria. This mismatch makes it difficult to assess whether features like broad lines, steep optical slopes, or extreme Balmer breaks are common or limited to specific subsets.

In this paper, we address these issues by constructing a large, uniformly selected sample of photometric LRDs across six JWST deep fields. In § 3, we apply an inclusive, color-based selection that recovers the full photometric diversity reported in previous studies, including sources missed by more restrictive criteria. We then cross-match this sample with all available NIRSpec spectroscopy compiled in the Dawn JWST Archive (DJA)¹, enabling a systematic comparison between photometric and spectroscopic properties. In § 4, we use continuum spectroscopy to measure rest-frame UV and optical slopes and colors, free from emission-line contamination, and to characterize population-wide correlations among these quantities. Finally, in § 5, we interpret these

trends within a semi-empirical two-component model combining a galaxy and a BH* component, demonstrating that it naturally reproduces the observed range of LRD continuum and emission-line properties.

Throughout the paper, we assume a flat cosmology with $\Omega_M = 0.3$, $\Omega_\Lambda = 0.7$, and a Hubble constant $H_0 = 70 \text{ km s}^{-1} \text{ Mpc}^{-1}$. We use AB magnitudes (Oke & Gunn 1983).

2. DATA

2.1. JWST/NIRCam Photometry

For source identification and photometry in the CEERS-EGS, PRIMER-UDS, PRIMER-COSMOS, and UNCOVER fields, we use version v7.2 of the publicly available photometric catalogs from the DJA. These catalogs are derived from JWST/NIRCam Level-2 imaging processed with the grizli pipeline (Brammer 2019), including PSF-matching across filters. Source detection is performed using SEP (Barbary et al. 2015), a Python implementation of SExtractor (Bertin & Arnouts 1996), applied to a detection image typically based on F444W. Photometry is measured in $0''.5$ diameter circular apertures and corrected to total flux using Kron scaling (Kron 1980), with filter-dependent aperture corrections applied based on empirical PSFs (see Valentino et al. 2023 and Brammer et al., in prep., for details). For the JADES fields (GOODS-N and GOODS-S), we use the official Data Release 3 (DR3) multi-band photometric catalogs (Eisenstein et al. 2023; D’Eugenio et al. 2025b), which include consistent photometry across NIRCam bands based on the JADES pipeline.

2.2. JWST/NIRSpec Spectroscopy

For NIRSpec spectroscopy, we focus primarily on low-resolution ($R \sim 100$) PRISM observations, as our primary goal is to characterize the continuum shapes of LRDs. Some results based on higher-resolution grating data are also discussed where relevant. Spectra are drawn from version 4.4 of the DJA, which compiles uniformly reduced NIRSpec data across all major extragalactic surveys. Reductions were performed with the latest version of the open-source pipeline `msaexp` (Brammer 2023), as described in de Graaff et al. (2024) and Heintz et al. (2025). The DJA processing includes background subtraction, flat-fielding, 2D rectification, and optimal 1D extraction, along with masking of contaminated regions and quality flags for each pixel. All spectra include associated error, contamination flags, and metadata for reproducibility.

Specifically, we cross-match source with robust spectroscopic redshift (grade=3) in the DJA spectroscopic table with photometric catalogs in each field using a

¹ <https://dawn-cph.github.io/dja>

0''.5 matching radius to identify spectra corresponding to photometrically selected LRDs (see next section). Approximately three-quarters of the spectra come from three large programs: the Red Unknowns: Bright Infrared Extragalactic Survey (RUBIES; GO-4233; de Graaff et al. 2024), and the CANDELS-Area Prism Epoch of Reionization Survey (CAPERS; GO-6838; PI: Dickinson), which target the CEERS-EGS, PRIMER-UDS, and PRIMER-COSMOS (CAPERS only) fields, and the JWST Advanced Deep Extragalactic Survey (JADES; GTO-1180, 1181, 1286; Curtis-Lake et al. 2025; Scholtz et al. 2025) covering GOODS-N and GOODS-S. These contribute 30, 28, and 30 spectra to our sample, respectively (25%, 23%, and 25%). An additional 11 LRDs ($\sim 10\%$) come from spectroscopic follow-up in the UNCOVER field (GO-2561; Bezanson et al. 2024). The remaining 20 sources ($\sim 17\%$) are drawn from a range of smaller programs, including GTO-1215 (Maseda et al. 2024), GO-5224 (Naidu et al. 2025), CEERS (GO-1345; Finkelstein et al. 2025), DDT-2750 (PI: Arrabal Haro), GO-4106 (PIs: Nelson & Labbe), GO-6585 (PI: Coulter), GO-3073 (PI: Castellano), DDT-6541 (PI: Egami), and GO-2198 (PI: Baruffet).

3. PHOTOMETRIC SELECTION OF LRDS

3.1. Selection criteria and completeness

We identify LRDs using the photometric selection method introduced by Barro et al. (2024b), applied uniformly across six JWST deep fields. Briefly, we use an observed color-color criterion (F200W–F444W vs. F115W–F200W) designed to identify the characteristic blue UV and red optical SEDs of LRDs. The selection region boundaries are defined to encompass the redshift-color tracks of representative LRDs spanning a broad range of rest-frame colors at $z \gtrsim 3$. We use F200W, rather than the previously adopted F277W, as the pivot filter to better sample the rest-frame UV at lower redshifts and avoid contamination from emission lines in both color axes. As in prior work, we also apply a compactness cut based on the flux ratio in two small apertures ($F444W[0''.5]/F444W[0''.2] < 1.5$).

This approach captures nearly all candidates identified by the selection criteria of Kocevski et al. (2024) and Kokorev et al. (2024a), while recovering an additional $\sim 20\%$ of sources with bluer UV-to-NIR colors that fall outside those earlier definitions. Although optimized for completeness at $z \sim 3$ –7, the selection becomes increasingly incomplete at higher redshifts ($z \gtrsim 8$), where the F150W–F200W color begins to trace the Lyman break, shifting sources out of the selection region. Nonetheless, this method probes a broader region of color-color

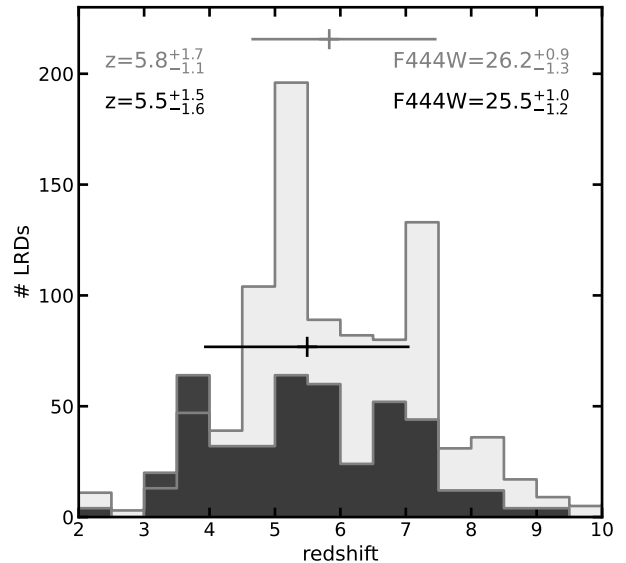


Figure 1. Redshift distribution of the photometric LRD sample (gray) and the NIRSpec/PRISM spectroscopic subset (black, scaled by a factor of 3). Horizontal lines show the median redshift and percentiles for each sample. The full sample spans $z \sim 3$ –9 with peaks at $z \sim 5$ and $z \sim 7$; the spectroscopic subset is skewed slightly lower, likely due to selection biases in spectroscopic follow-up favoring brighter sources.

space, providing the most inclusive and comprehensive sampling of the photometric diversity within the LRD population.

Overall, we identify ~ 1000 LRDs down to a limiting magnitude of $F444W = 27.5$ (28 in the JADES fields), including 191 LRDs with NIRSpec/PRISM spectra in DJA over an area of 632.4 arcmin^2 . Approximately 70% of the spectra have sufficient signal-to-noise in the rest-frame UV and optical continuum for SED fitting (see § 4 and 5). Sample sizes by field are summarized in Table 1. Figure 1 shows the redshift distribution for the full photometric LRD sample (gray) and the NIRSpec/PRISM spectroscopic subset (black, scaled by a factor of 3). The photometric sample spans a wide range from $z \sim 3$ to 9, with two prominent peaks at $z \sim 5$ and $z \sim 7$, and a median redshift of $z = 5.8^{+1.7}_{-1.1}$. This is consistent with Barro et al. (2024b), but our analysis expands the sample from 248 to nearly 1000 LRDs and extends coverage to all six JWST deep fields. As in Barro et al. (2024b), the lower-redshift peak is partly driven by LRDs with bluer optical colors and strong $[\text{OIII}]\lambda 5007$ emission that boosts F277W; these are recovered by our selection and by Kokorev et al. (2024a), but are largely missed by redder cuts such as those in Kocevski et al. (2024), which yield a higher median redshift of $z \sim 6.4$. In contrast, our selection becomes increasingly incomplete at $z \gtrsim 8$,

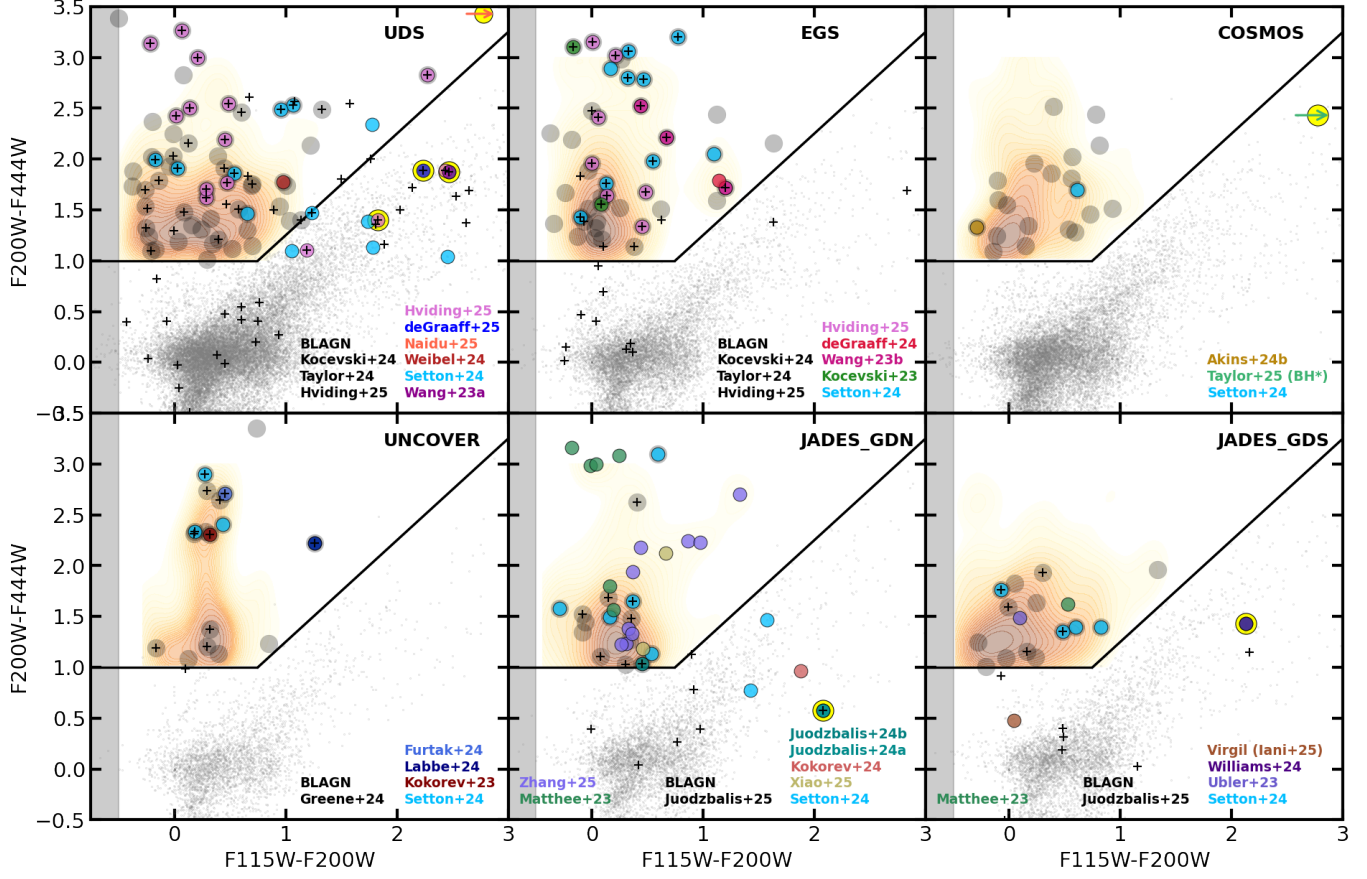


Figure 2. Color–color selection diagram of LRDs based on the Barro et al. (2024b) criterion (solid lines; gray area to reject brown dwarf contaminants) for the six JWST deep fields analyzed in this work. Small gray dots show the full photometric catalog, while the orange density map marks the distribution of sources selected as photometric LRDs. Gray circles indicate LRDs with high-quality NIRSpec/PRISM spectra from DJA. Colored symbols highlight literature LRDs within this sample; when an object appears in multiple studies, only the original reference is shown. Black crosses denote sources classified as BLAGNs in previous studies. Yellow circles indicate compact spectroscopic LRDs that were missed by the photometric selection and were added manually for completeness. The diagram demonstrates that the vast majority of previously identified spectroscopic LRDs fall within the photometric selection region.

where the F150W–F200W color begins tracing the Lyman break. The spectroscopic subset shows a slightly lower median redshift of $z = 5.5_{-1.6}^{+1.5}$, likely reflecting selection biases toward brighter targets more easily observed in follow-up. This is consistent with their brighter median $F444W = 25.5$, compared to 26.2 for the full photometric sample.

Figure 2 shows the LRD color–color selection diagram from Barro et al. (2024b) for all six fields, with the photometric LRD population shown as an orange density map and spectroscopic LRDs as gray circles. Most spectroscopically identified LRDs from the literature fall within our photometric selection region, demonstrating excellent agreement between photometric and spectroscopic classifications. This includes all NIR-Cam/WFSS BLAGNs from Matthee et al. (2024) and $\sim 76\%$ of the red, high-equivalent-width ($EW > 400\text{\AA}$)

sources from Setton et al. (2024). The remaining $\sim 20\%$ are predominantly extended sources (Setton et al. 2024) with red rest-frame UV–optical SEDs characteristic of dusty, massive galaxies (e.g., 6585-COS-60504, RUBIES-UDS-41598, RUBIES-UDS-152282, RUBIES-UDS-19735, WIDE-GDN-6406). Excluding these extended sources increases the selection completeness to 87%.

There are, however, a small number of compact, spectroscopic LRDs with broad emission lines that are missed by our photometric selection, as well as by most other criteria. These sources typically have relatively low redshifts ($z \lesssim 3$) and/or unusually red rest-frame UV slopes, which shift their F115W–F200W colors out of the LRD selection region and into the locus of massive dusty galaxies (see Figure 1 of Barro et al. 2024b). We identify seven such objects in the literature and in-

clude them manually in the photometric sample for completeness; they are marked with yellow circles in Figure 2. Notably, RUBIES-BLAGN-1 (Wang et al. 2024b), JADES-1180-12402 (Setton et al. 2024; Williams et al. 2023), the “Rosetta” AGN (Juodžbalis et al. 2024a), and RUBIES-UDS-144195 (Hviding et al. 2025) are among the lowest-redshift LRDs, at $z = 3.11, 3.19, 2.26,$ and $3.404,$ respectively. All but the “Rosetta” source show significantly redder UV slopes (see discussion in § 4). We additionally include the three reported extreme Balmer break sources (“black hole stars”, BH*) from de Graaff et al. (2025a), Naidu et al. (2025), and Taylor et al. (2025), which exhibit weak UV emission and are identified solely by their extremely red optical colors.

While the addition of these six spectroscopic LRDs contributes negligibly to the overall photometric sample, and less than 1% to the spectroscopic one, they highlight the need for a more complete diagnostic criterion based on rest-frame continuum properties. Classification using rest-frame UV and optical slopes (Kocevski et al. 2024; Hainline et al. 2024) or UV-to-optical colors (Barro et al. 2024a) offers a more robust way to organize and distinguish LRD subtypes. As we show in § 4, these six sources fall at the red end of the rest-frame color diagram but are otherwise consistent with the broader LRD population.

Rest-frame colors or slopes provide a redshift-independent and physically motivated method for identifying LRDs based on their distinctive SED shapes, similar to how the UVJ diagram (Wuyts et al. 2007; Williams et al. 2010) separates quiescent, dusty, and star-forming galaxies. However, such classifications depend critically on how rest-frame properties are derived. The most reliable approach would use low-resolution, broad-wavelength spectroscopy (e.g., NIR-Spec/PRISM), which clearly separates continuum and line emission. However, while low-resolution spectra are only available for limited samples, broad photometric coverage extending into the mid-IR (e.g., NIRC*am* + MIRI F560W/F770W) can effectively trace the rising optical SED even at $z \gtrsim 6$ and mitigate contamination from strong emission lines in NIRC*am* bands (especially F277W, F356W, and F444W).

A key limitation of color-based selections in discrete redshift bins, such as that used by Kocevski et al. (2024), is that individual bands can be biased by line contamination (e.g., F277W at $z \sim 5$; see Barro et al. 2024a), resulting in incompleteness. By contrast, fitting the full photometric SED at the best available redshift allows for interpolation across uncontaminated bands or SED modeling with templates that include emission lines,

yielding more reliable estimates of the intrinsic continuum slope or color.

3.2. Other compact, non-LRD sources

Compact quiescent galaxies represent another population that can overlap with and contaminate LRD selections. These sources share key observable features, red colors, compact morphologies, and, in some cases, broad emission lines (Kocevski et al. 2023b), but their intrinsic SEDs differ markedly from those of LRDs. Specifically, quiescent galaxies exhibit red UV slopes, and while their optical continua are steep near the Balmer break, they flatten rapidly at longer wavelengths, deviating from the approximate power-law behavior typical of LRDs.

Figure 2 highlights the locations of three recently reported quiescent galaxies at high redshift from KokoREV et al. (2024a), Weibel et al. (2024), and de Graaff et al. (2024) in the photometric selection diagram. The latter two fall within the LRD selection region near its red boundary, making them potential contaminants. This occurs because, at $z > 5$, the F200W band samples wavelengths blueward of the Balmer break, causing F200W–F444W colors to appear redder and F115W–F200W colors bluer, thereby pushing quiescent galaxies into the LRD selection box. In the next section, we demonstrate that a rest-frame color–color diagram can effectively distinguish these contaminants based on their distinct SED shapes.

Another interesting source is “Virgil”, a spectroscopically confirmed Lyman- α emitter at $z=6.6$ in JADES-GDS (Iani et al. 2024; Rinaldi et al. 2025), which exhibits a rest-frame UV–optical SED typical of LAEs at similar redshifts. In NIRC*am* bands, its SED is entirely blue and would place it well outside the standard LRD selection region, in the lower-left corner of the photometric diagram. However, MIRI photometry reveals a steeply rising red continuum beyond rest-frame $\sim 0.7\mu\text{m}$, producing an optical-to-NIR slope similar to that seen in LRDs. If rest-frame colors incorporating these longer-wavelength data were used, “Virgil” would fall within the LRD color space. This example highlights the possibility of a hidden population of LRD-like sources that are missed by traditional NIRC*am*-based selections. It suggests a possible scenario in which the component dominating the rest-frame optical emission, likely an exotic type of AGN or compact dusty star formation, can vary in luminosity relative to a relatively blue, UV-dominated host, producing a continuum of UV–NIR colors. We explore this connection further in the next section using a rest-frame color–color diagram.

3.3. Spectroscopic samples of BLAGNs

Field	Area (arcmin ²)	Phot. LRDs	Spec. LRDs	S/N _{UV} > 2	BLAGNs LRDs	LRDs BL
CEERS-EGS	88.6	127	45	25	61%	89%
PRIMER-UDS	243.0	353	68	33	59%	89%
JADES-GDS	62.1	92	21	17	50%	70%
JADES-GDN	56.0	112	19	16	67%	54%
UNCOVER	43.8	45	14	12	92%	65%
PRIMER-COSMOS	138.9	207	23	15	N/A	N/A
Total	632.4	968	191	118	-	-

Table 1. Summary of LRD and AGN statistics by field, including photometric and spectroscopic sample sizes, and the fraction of BLAGNs classified as LRDs and LRDs with broad emission lines.

Figure 2 shows the distribution of a large compilation of broad-line AGNs (BLAGNs) from the literature in the photometric selection diagrams for each field (black crosses). These samples are primarily based on NIRSpec grating observations (Kocevski et al. 2023a; Harikane et al. 2023; Kocevski et al. 2024; Maiolino et al. 2023; Taylor et al. 2024; Hviding et al. 2025), prism spectra (Greene et al. 2024), and NIRCam/WFSS data (Matthee et al. 2024). The goal is to quantify (i) what fraction of BLAGNs are identified as LRDs by photometry, and (ii) what fraction of photometric LRDs exhibit broad lines.

In CEERS-EGS, we compile BLAGN measurements from Kocevski et al. (2023a), Harikane et al. (2023), Kocevski et al. (2024), Taylor et al. (2024), and Hviding et al. (2025). The first two studies identified BLAGNs using data from the CEERS spectroscopic program. Kocevski et al. (2024) extended this work using early observations from the RUBIES program. Hviding et al. (2025) and Taylor et al. (2024) further expanded the sample, conducting more comprehensive searches for broad H α emission using the full RUBIES and combined RUBIES+CEERS datasets, respectively. Consequently, the Hviding et al. (2025) and Taylor et al. (2024) samples are the largest. We identify 25 of the 28 BLAGNs from Taylor et al. (2024) within the area covered by our photometric catalog, and all 28 from Hviding et al. (2025). Combined, these yield 40 unique BLAGNs, with only \sim 30% (13) in common between the two samples. All 8 sources from Kocevski et al. (2024), and all but one from Harikane et al. (2023), are also included in this combined set. Including the additional Harikane et al. (2023) source brings the total to 41 BLAGNs. Of these, 25 (61%) satisfy our photometric LRD selection.

A fraction of 61% (25/41) of BLAGNs classified as photometric LRDs is notably higher than the \sim 34% reported in Taylor et al. (2024) and the \sim 54% in Hviding et al. (2025). The larger discrepancy with Taylor et al. (2024) arises because their analysis identified photometric LRDs using only the less complete Kocevski

et al. (2024) sample. The difference with Hviding et al. (2025) likely stems from the inclusion of bluer LRDs in our selection. Their classification relies on a combination of compact morphology, broad-line emission, and a “V-shaped” SED. The latter requires a spectroscopic optical slope of $\beta_{\lambda, \text{OPT}} > 0$ (i.e., $\beta_{\nu, \text{OPT}} > 2$), similar to the threshold in Kocevski et al. (2024), whereas our method extends to bluer slopes (see next section). In turn, all of the spectroscopic LRDs (15) in Hviding et al. (2025) are photometric LRDs by our selection.

Estimating the fraction of LRDs that exhibit broad lines is more complex, as it depends on knowing which photometric LRDs were analyzed in BLAGN surveys with sufficiently deep spectra for BLAGN identification. To compare with the more complete samples from Hviding et al. (2025) and Taylor et al. (2024), we identify photometric LRDs with reliable (grade=3 in DJA) G395M grating spectra from RUBIES and redshifts in the range $3.5 < z < 6.8$, ensuring that H α falls within the spectral coverage. We find 19 such LRDs, of which 17 (89%) exhibit broad lines. The two exceptions, RUBIES-EGS-69475 and -57375, have very low S/N in the optical continuum, which may prevent reliable linewidth measurements. One additional LRD (RUBIES-EGS-9809) lacks a broad-line classification because H α falls in the chip gap.

In UDS, we again use BLAGN samples from Kocevski et al. (2024), Taylor et al. (2024), and Hviding et al. (2025), all based on spectra from the RUBIES survey. We identify all 35 sources in Taylor et al. (2024), 50 of 51 from Hviding et al. (2025), and 6 from Kocevski et al. (2024). The combined Taylor et al. (2024) and Hviding et al. (2025) samples yield a total of 69 unique BLAGNs, with only \sim 25% (17) overlapping between them. Adding two additional sources found only in Kocevski et al. (2024) brings the total to 71. Of these, 42 (59%) satisfy our photometric LRD criterion. This fraction is again higher than those reported in Taylor et al. (2024) and Hviding et al. (2025), which are 34% and 40%, respectively.

We also find that 19 of the 20 spectroscopic LRDs from [Hviding et al. \(2025\)](#) within our photometric catalog are classified as photometric LRDs. However, three of these were manually added due to their combination of lower redshift and/or red UV slopes that make them fall outside our photometric selection (RUBIES-BLAGN1, “The Cliff”, and RUBIES-144195; see previous section). The one remaining exception, RUBIES-33938, is relatively faint with a low S/N spectrum, has a moderate color ($F277W-F444W \sim 1$ mag), and is not identified as a photometric LRD in any prior studies.

Among LRDs with good-quality G395M grating spectra from RUBIES and spectroscopic redshifts between $3.5 < z < 6.8$, we identify 36 sources. Of these, 32 (89%) are classified as BLAGNs in the literature. The remaining four: RUBIES-166271, 40800, 59492, and 125917, have low optical S/N, which complicates reliable line width measurements and does not rule out the presence of faint broad lines.

In JADES-GDS and GDN, we use BLAGN identifications from [Juodžbalis et al. \(2025\)](#), based on multiple GTO spectroscopic programs in the JADES fields. Most of these measurements rely on R1000 grating data, primarily G395M, with G235M used at lower redshift. The sample includes 12 BLAGNs from [Maiolino et al. \(2023\)](#) and one from [Matthee et al. \(2024\)](#). In GDS, we identify 14 of the 16 BLAGNs in [Juodžbalis et al. \(2025\)](#); the other two are either outside the photometric mosaic or blended with a foreground galaxy. Of the 14, seven (50%) satisfy the photometric LRD selection. To estimate the LRD fraction with broad lines, we identify ten LRDs with good-quality grating spectra ($z < 6.8$), of which seven (70%) show broad lines in [Juodžbalis et al. \(2025\)](#). In GDN, we identify all 15 BLAGNs in [Juodžbalis et al. \(2025\)](#), of which 10 (67%) are photometric LRDs. We also find 13 LRDs with grating spectra at $z < 6.8$, of which seven (54%) have broad lines. For completeness, we note that all seven BLAGNs in JADES-GDS and GDN identified by [Matthee et al. \(2024\)](#) also satisfy the LRD photometric selection.

In UNCOVER, we use the BLAGN sample from [Greene et al. \(2024\)](#). This field differs from the others in that the broad-line measurements are based on lower-resolution, but typically higher-S/N, NIRSpect prism data rather than gratings. We identify all 12 sources in the sample, of which 11 (92%) satisfy the photometric LRD selection (ID 35488 lies just outside the selection boundary). To estimate the spectroscopic overlap, we identify 17 photometric LRDs that were targeted by the UNCOVER spectroscopic program; of these, 11 (65%) are classified as BLAGNs in [Greene et al. \(2024\)](#).

In PRIMER-COSMOS, no large-scale spectroscopic programs for BLAGN identification are currently available. The ongoing CAPERS program (PI: Dickinson) may provide this information in the future, but only from PRISM data.

Overall, we find that the fraction of LRDs among samples of BLAGNs is relatively high, typically ranging from 60% up to 90% in UNCOVER. These values are higher than those reported in earlier studies using the same BLAGN samples, primarily due to (1) the adoption of a more flexible photometric selection that extends to bluer UV-to-optical colors (i.e., shallower optical slopes), and (2) the inclusion of a small number of spectroscopic LRDs at lower redshift that fall outside traditional color cuts. For example, [Taylor et al. \(2024\)](#) report an LRD fraction of $\sim 34\%$ among BLAGN in CEERS-EGS and PRIMER-UDS, while [Hainline et al. \(2024\)](#) find a value of $\sim 30\%$ in JADES after excluding three LRD-targeted sources. Indeed, the spectroscopic follow-up strategy plays a significant role in these differences. The 90% fraction in UNCOVER reflects a strong targeting bias, as many sources were selected specifically to follow up the LRDs identified in [Labbé et al. \(2023\)](#). Similarly, the RUBIES survey prioritized red NIRCcam sources, which naturally favors LRD-like objects. As noted by [Greene et al. \(2024\)](#), both the equivalent width and FWHM of broad lines tend to be larger in the reddest sources (e.g., $F277W-F444W > 1.6$), making BLAGNs that are also LRDs easier to detect. [Hainline et al. \(2024\)](#) and [Zhang et al. \(2025\)](#) reach a similar conclusion, showing that LRDs dominate the high-luminosity end of the AGN population. Consequently, it is clear that larger, unbiased spectroscopic samples are needed to reliably assess the intrinsic fraction of LRDs among the full BLAGN population.

The fraction of LRDs with broad emission lines is also relatively high, typically around 50–90%. Importantly, these values represent lower limits, as nearly all LRDs show clear emission lines, and the identification of broad components is often limited by the depth and sensitivity of the observations.

4. REST-FRAME UV SLOPES AND OPTICAL COLORS

This section analyzes the distribution of spectroscopic LRDs in a rest-frame color versus slope diagram that characterizes their UV and optical continuum shapes. In the following subsections, we use this diagram as a framework to classify the LRD population and investigate trends in their SEDs, including the shape of the continuum and the properties of their emission lines such as FWHM, flux ratios, and equivalent widths.

4.1. Rest-frame color - slope diagram classification

Here, we analyze a subset of 118 LRDs (out of 191) with NIRSpec/PRISM spectroscopy and high S/N continuum in the UV. We require an average S/N per pixel > 2 in the range $\lambda_{UV} = 1200 - 3500 \text{ \AA}$. Since LRDs are typically red, this threshold also implies higher S/N in the optical, ensuring sufficient signal for reliable SED modeling. We compute UV slopes by fitting a power law to the continuum between the Lyman and Balmer limits, using the convention $f_\nu \propto \lambda^{\beta_\nu}$. The slope is measured in f_ν rather than the traditional f_λ , where $\beta_\nu = \beta_\lambda + 2$, to enable direct comparison with the rest-frame UV-to-optical color, $[0.3-0.9 \mu\text{m}]$, defined using synthetic tophat filters of width 100 \AA .

To characterize the optical continuum, we adopt a rest-frame color rather than a formal slope. As noted in previous studies, many LRDs show significant continuum curvature and strong Balmer breaks (e.g., Wang et al. 2024a; Furtak et al. 2023; Labbe et al. 2024; Setton et al. 2024), making simple power-law slopes inadequate. Figure 3 illustrates one such case: A2744-45924 (Labbe et al. 2024), which exhibits a prominent Balmer break. The optical slope measured redward of H_∞ (green line) underestimates the true curvature and fails to capture the discontinuity. In contrast, the $[0.3-0.9 \mu\text{m}]$ color spans a broader wavelength baseline across the Balmer break and reflects those features more robustly. As a result, LRDs with prominent breaks often have $[0.3-0.9 \mu\text{m}]$ colors that exceed what their optical slope would predict.

For comparison with earlier work, this rest-frame optical color can be interpreted approximately as a two-point slope, with a numerical relation similar to:

$$\beta_{\nu, \text{OPT}} = \frac{0.4(m_{0.3} - m_{0.9})}{\log(0.3 \mu\text{m}/0.9 \mu\text{m})} = 1.2 \cdot [0.3-0.9 \mu\text{m}] \quad (1)$$

Figure 4 shows the distribution of UV slope versus rest-frame optical color ($[0.3-0.9 \mu\text{m}]$) for the LRD sample. Spectroscopic LRDs are shown as grey circles, while orange density contours represent the broader photometric sample, with slopes and colors derived from best-fit SEDs. This diagram conveys similar information to the UV and optical slope classifications proposed by Kocevski et al. (2024) and Hainline et al. (2025), but based here on continuum spectroscopy. The top and right histograms show the UV slope and optical color distributions for the photometric (orange) and spectroscopic (black) samples. Vertical and horizontal dashed lines indicate the Kocevski et al. (2024) slope thresholds ($\beta_{\nu, \text{OPT}} > 2$; $\beta_{\nu, \text{UV}} > 1.27$), while the dashed-dotted line marks the approximate limit used by Barro et al.

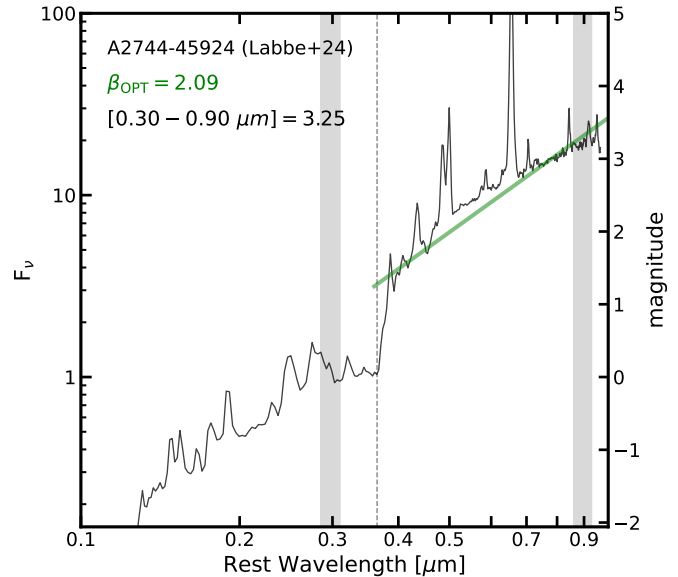


Figure 3. Example of an LRD with a prominent Balmer break illustrating the difference between the optical slope and the rest-frame UV-to-optical color. The black line shows the NIRSpec/PRISM continuum spectrum, with a green line indicating the best-fit power law to the optical continuum redward of the Balmer limit (H_∞). The shaded gray regions mark the wavelength ranges used to compute the $[0.3-0.9 \mu\text{m}]$ color. In LRDs with prominent continuum breaks, the rest-frame color is often significantly larger than the optical slope, as the latter fails to capture the presence of a sharp discontinuity.

(2024a) ($F277W-F444W > 1.5$; $\beta_{\nu, \text{OPT}} \gtrsim 3$). Colored symbols mark prominent LRDs from previous studies.

The median optical color of the photometric LRDs is $[0.3-0.9 \mu\text{m}] = 2.3^{+0.9}_{-0.7} \text{ mag}$, but the population spans nearly 4 magnitudes in color, showing that LRDs comprise a diverse set of sources with likely varied intrinsic properties. The selection used by Barro et al. (2024b) includes many bluer LRDs with optical slopes below the typical threshold of Kocevski et al. (2024), comprising the bottom $\sim 30\%$ of the sample. These include well-studied sources like those in Akins et al. (2024b), Juodžbalis et al. (2024a), and “Virgil,” which was confirmed as an LRD only after incorporating MIRI data. These bluer LRDs are critical for probing the boundary between LRDs and normal galaxies, where the AGN becomes subdominant. At the red end, LRDs selected with a stricter observed color cut ($F277W-F444W > 1.5$; $[0.3-0.9 \mu\text{m}] \gtrsim 3$), as in Barro et al. (2024a) and Akins et al. (2024a), make up only the top 18% of the sample and do not include the median LRD. Beyond this

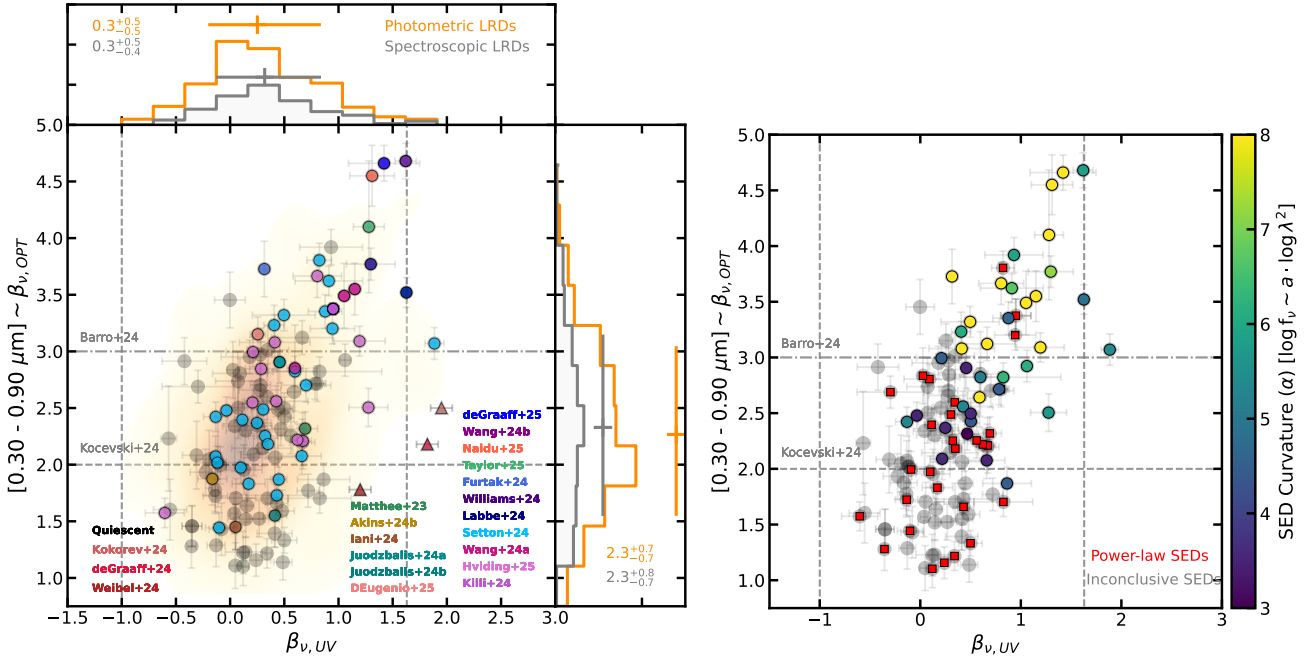


Figure 4. Rest-frame UV slope versus optical color for LRDs with high-S/N ($S/N_{UV} > 2$) NIRSpec/Prism continuum detections. *Left:* Distribution for 118 spectroscopic LRDs. Colored markers highlight sources from the literature, including those reported to show strong continuum breaks near the Balmer limit (e.g., Wang et al. 2024a; Furtak et al. 2024; Labbe et al. 2024; de Graaff et al. 2025a; Naidu et al. 2025; Taylor et al. 2025). Dashed and dashed-dotted lines indicate selection thresholds from Kocevski et al. (2024) and Barro et al. (2024a). Orange density contours and histograms show the full photometric LRD sample using SED-fit values; gray histograms show the same for the spectroscopic subset. Medians and 68% percentiles for both samples are indicated. The LRD population spans nearly 4 magnitudes in $[0.3-0.9 \mu\text{m}]$ color, reflecting substantial diversity in their SEDs. Most LRDs have blue UV slopes ($\beta_{\nu,UV} = 0.3^{+0.5}_{-0.5}$), but there is a clear trend toward redder UV slopes at redder colors, reaching $\beta_{\nu,UV} \sim 1$ for the reddest 7% with $[0.3-0.9 \mu\text{m}] > 3.5$. *Right:* Same color–slope diagram, now color-coded by the curvature of the rest-optical continuum, computed from second-degree polynomial fits to the log-log SEDs. Red squares mark LRDs best fit by power laws. Strongly curved SEDs (yellow) are concentrated among the reddest LRDs, while bluer LRDs typically exhibit power-law-like continua. Some overlap remains around the median $[0.3-0.9 \mu\text{m}]$ color (see discussion in § 4.4).

threshold, the number density drops quickly. The most extreme cases, with $[0.3-0.9 \mu\text{m}] \gtrsim 3.5$, represent just 7% of the population, yet include most of the prominent LRDs in the literature. While these have been critical to shaped our understanding of the population, they are not representative but rather occupy the red extreme of the distribution.

Figure 4 also shows a clear trend toward redder UV slopes at higher $[0.3-0.9 \mu\text{m}]$. Most LRDs follow the canonical “V-shaped” SED with blue UV slopes ($\beta_{\nu,UV} = 0.3^{+0.5}_{-0.5}$) and red optical colors, but among redder sources, the UV slope steepens. For photometric LRDs with $[0.3-0.9 \mu\text{m}] > 3$ and > 3.5 , the median UV slope increases to $\beta_{\nu,UV} = 0.6^{+0.4}_{-0.6}$ and $0.8^{+0.4}_{-0.3}$, respectively. Among spectroscopic LRDs, the trend is even stronger, with medians of $0.9^{+0.4}_{-0.4}$ and $1.0^{+0.6}_{-0.2}$ in the same bins. These include several well-studied LRDs known for their strong continuum breaks near the Balmer limit (Wang et al. 2024a; Furtak et al. 2023; Labbe et al. 2024;

de Graaff et al. 2025a; Naidu et al. 2025; Taylor et al. 2025), all with UV slopes $\beta_{\nu,UV} \gtrsim 1$.

This trend poses a challenge for photometric selections, which are tuned to detect the combination of blue UV and red optical slopes. Instead, the reddest LRDs begin to resemble quiescent or dusty galaxies with uniformly red continua, making them harder to identify in standard color–color diagrams (as noted in Section 3.1). Several LRDs with red UV slopes were thus identified only a posteriori from spectroscopy (Wang et al. 2024a; Juodžbalis et al. 2024a; Williams et al. 2024). Yet once placed on the color–slope diagram, they fall well within the main LRD distribution, supporting their classification as true LRDs.

In contrast, candidate quiescent galaxies from Weibel et al. (2024), Kokorev et al. (2024b), and de Graaff et al. (2025b) lie significantly outside the LRD locus. Although some have red optical colors ($[0.3-0.9 \mu\text{m}] \sim 2-2.5$ mag), they show much redder UV slopes ($\beta_{\nu,UV} \gtrsim 1$) than LRDs with similar colors. This sepa-

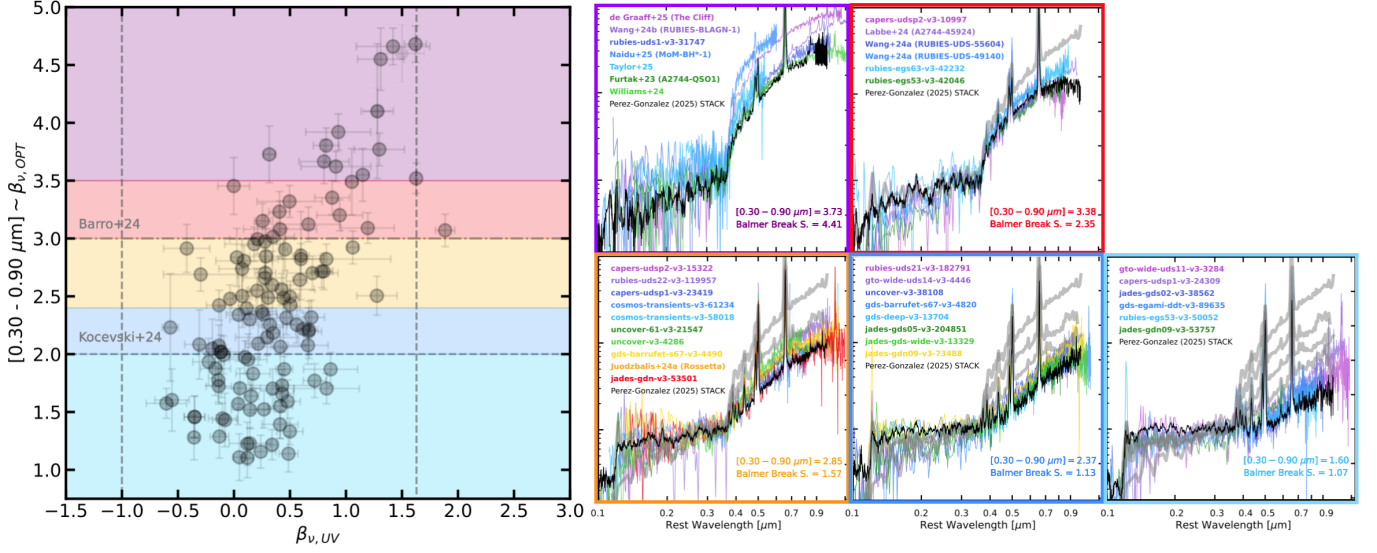


Figure 5. *Left:* Same color–slope diagram as in Figure 4, now divided into five bins of $[0.3\text{--}0.9\ \mu\text{m}]$ color from reddest to bluest. *Right:* Top to bottom, the five panels show individual spectra of representative LRDs with high continuum S/N in each color bin, highlighting the diversity in SED shapes. Black lines show stacked LRD spectra from Perez-Gonzalez (in prep.) for the same bins. Gray lines show the stacked spectra from redder bins, carried forward to each panel to highlight differences across the sequence. The reddest LRDs (top two panels; $[0.3\text{--}0.9\ \mu\text{m}] > 3$, $\sim 20\%$ of the sample) exhibit strong Balmer breaks, pronounced curvature, and redder UV slopes. Toward bluer LRDs (bottom three panels), the breaks and curvature diminish, giving way to smoother, power-law-like SEDs. The UV slope also becomes markedly bluer, with median values near $\beta \sim 0.3$ across all three bluest bins.

ration highlights the utility of the color–slope diagram for distinguishing LRDs from quiescent interlopers in photometric samples.

4.2. Curvature vs. power-law in the rest-optical SED

We use the detailed spectral coverage of the optical SED provided by NIRSPEC/PRISM to examine the continuum shape of LRDs. Our goal is to quantify what fraction of the population shows significant curvature or breaks in the optical, which may point to stellar-dominated SEDs (e.g., Williams et al. 2024; Pérez-González et al. 2024), or more exotic BH* or quasi-stellar components (e.g., Inayoshi & Maiolino 2024; Naidu et al. 2025). These cases differ from the smoother power-law continua often associated with canonical obscured AGNs in broadband photometry (e.g., Polletta et al. 2006).

To quantify these differences without relying on specific physical models, we fit the rest-frame SEDs in $\log(f_\nu)\text{--}\log(\lambda)$ space using two simple functions: (1) a linear model representing a power-law ($a \cdot \log \lambda$), and (2) a second-degree polynomial ($a \cdot \log \lambda^2 + b \cdot \log \lambda$) that captures curvature. We compare the fits using both χ^2 and the Akaike Information Criterion (AIC). For spectra better fit by the quadratic model, we use the coefficient a as a proxy for curvature strength. Sources with $a \sim 0$ are classified as power-law, while those with $a > 0$ but no strong AIC preference are labeled as inconclusive.

The right panel of Figure 4 shows the same color–slope diagram as the left, now color-coded by curvature for the best-fit quadratic models. Red markers indicate power-law SEDs, and grey circles mark inconclusive cases. The curved SEDs cluster toward the red end of the distribution ($[0.3\text{--}0.9\ \mu\text{m}] \gtrsim 3$), overlapping with LRDs previously reported to exhibit Balmer breaks. These sources show steep optical slopes with a sharp flattening toward the NIR, distinct from power-law shapes. In contrast, LRDs with bluer optical colors follow the typical “V-shaped” SED with blue UV and red optical power-law slopes.

A potential complication from this trend is that some of the reddest LRDs, despite lacking blue UV slopes or power-law continuum shapes, still show large differences between their UV and optical slopes. As a result, “V-shaped” metrics like $\Delta k = \beta_{\text{OPT}} - \beta_{\text{UV}}$ (e.g., Setton et al. 2024) can yield similar values for both curved and canonical blue plus red LRDs. This occurs because Δk runs diagonally across the color–slope diagram, grouping together sources from the top-right (strongly curved) and bottom-left (classical power-law) that have fundamentally different SED shapes.

4.3. The variety of SED types in LRDs

We further investigate the diversity of LRD SEDs as a function of rest-frame UV-to-optical color by examining both individual and median spectra for subsamples of

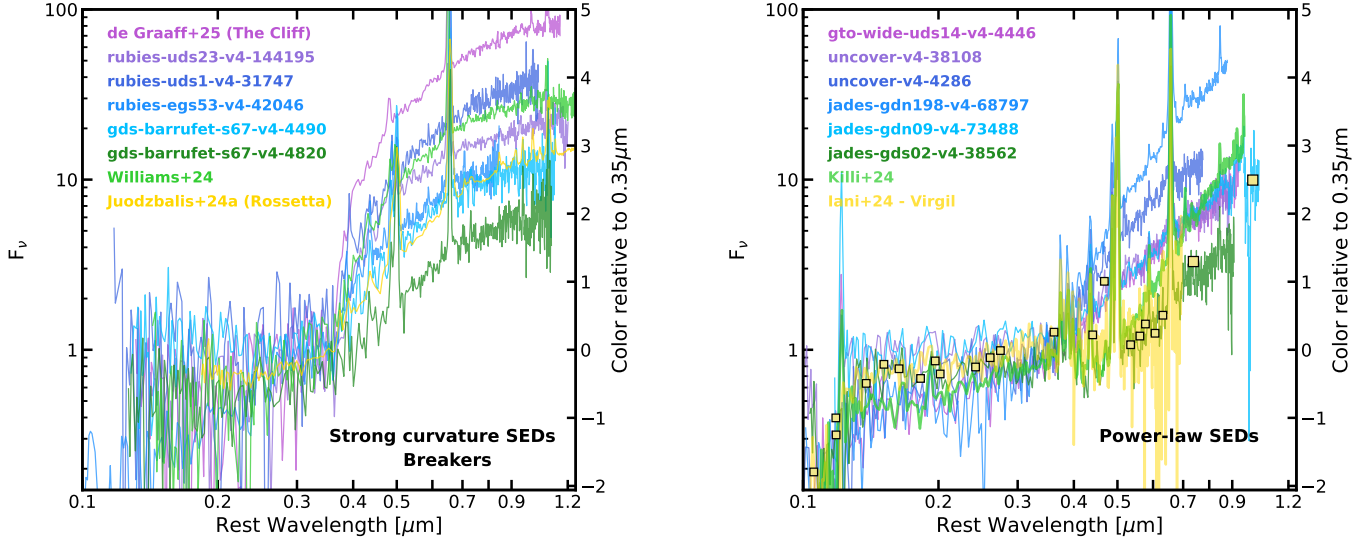


Figure 6. Examples of rest-frame spectra illustrating the two dominant spectral shapes among LRDs, strong curvature (“Breakers”) and power-laws, normalized at H_∞ . *Left:* LRDs with strong curvatures show SEDs that rise steeply redward of the Balmer limit followed by a flattening toward the NIR. *Right:* LRDs with power-law-like SEDs show smooth, constant slopes across the optical. While breakers typically have red $[0.3\text{--}0.9\ \mu\text{m}]$ colors and power-laws are generally bluer, there is overlap at intermediate colors—similar rest-frame colors can result from distinct SED shapes. In breakers, the optical continuum rises sharply at H_∞ , whereas in bluer power-law LRDs the inflection occurs at longer wavelengths. This is illustrated by “Virgil” (yellow), whose optical rise is delayed to $\sim 0.6\ \mu\text{m}$ and is visible only with MIRI photometry (large squares).

LRDs with high-S/N (>5) optical continuum. We divide the sample into five color bins spanning $[0.3\text{--}0.9\ \mu\text{m}] \sim 1$ to 5 mag. The bin widths are roughly 0.5 mag, adjusted slightly to include a similar number of sources per bin. The left and right panels of Figure 5 show the bin definitions and corresponding SEDs, all normalized at the Balmer limit (H_∞). The black line in each panel shows the median SED for each bin. The average color and Balmer break are also indicated.

The reddest bin ($[0.3\text{--}0.9\ \mu\text{m}] > 3.5$ mag) contains LRDs with the strongest curvature, reddest UV slopes, and most pronounced continuum breaks, with an average Balmer break strength of 4.41, far beyond what standard stellar population models can reproduce. This bin includes the three extreme LRDs from de Graaff et al. (2025a), Naidu et al. (2025), and Taylor et al. (2025) that motivated the black hole star (BH*) model, in which a dense gas cocoon surrounds an accreting black hole, causing the sharp decline. We further discuss this modeling in § 5. In addition to their breaks, these LRDs exhibit sharp flattening toward the NIR, consistent with the weak MIRI colors reported for the reddest LRDs (e.g., de Graaff et al. 2025a; Setton et al. 2025; Ronayne et al. 2025). The adjacent bin ($3 < [0.3\text{--}0.9\ \mu\text{m}] < 3.5$ mag) shows similar overall shapes, with somewhat weaker curvature, red UV slopes, and a lower average Balmer break amplitude of 2.35. This group includes some of the first spectroscopically confirmed LRDs with

strong but less extreme Balmer breaks (Kocevski et al. 2024; Labbe et al. 2024; Wang et al. 2024b). In both of the two reddest bins, LRDs tend to exhibit prominent, broad Balmer emission lines, with weaker or undetected metal lines. We discuss line ratios and equivalent widths in more detail in § 4.7.

The three bottom bins correspond to LRDs with $[0.3\text{--}0.9\ \mu\text{m}] < 3$, approaching the median color of the photometric sample ($[0.3\text{--}0.9\ \mu\text{m}] = 2.3$ mag). These sources display a remarkably similar flat UV continuum, with $\beta_{\nu, \text{UV}} \sim 0.3$, much bluer than in the redder bins. As $[0.3\text{--}0.9\ \mu\text{m}]$ decreases from 3 to 1, the average Balmer break amplitude declines steadily to 1.57, 1.13, and 1.07, values more typical of normal blue star-forming galaxies. Similarly, SED curvature diminishes toward shallower, power-law-like optical slopes. In these bins, the composite SED closely resembles the canonical combination of blue plus red power laws, with an inflection near the Balmer limit. In parallel, the median spectra show a growing prominence of narrow metal lines, especially the coronal lines around the Balmer break, such as $[\text{OII}]$ and $[\text{NeIII}]$, while the relative strength of $\text{H}\alpha$ appears to decline compared to the blended $\text{H}\beta + [\text{OIII}]\lambda 5007$ complex.

Notably, the median SEDs in the two bluest bins suggest that the inflection may occur redward of H_∞ , near the $[\text{OIII}]\lambda 5007$ emission line. This is consistent with “Virgil” (Iani et al. 2024; Rinaldi et al. 2025), a

blue LRD with a seemingly flat optical continuum that rises sharply beyond $H\alpha$. A shift in the inflection is quite relevant. One of the main arguments against two-component models (e.g., galaxy+AGN) has been the consistency of the inflection at H_∞ , which would favor a single-component origin (Setton et al. 2024). If the inflection point varies with color, it would instead favor a multi-component scenario for the peculiar SED of LRDs. We revisit this scenario in detail in § 5.

4.4. Breakers vs. Power-Laws: Diversity and Degeneracy in LRD SEDs

Figure 4 shows that redder LRDs tend to have more pronounced curvature in their optical SEDs, while bluer LRDs are more consistent with power-law shapes. However, there is some clear overlap. I.e., similar $[0.3\text{--}0.9 \mu\text{m}]$ colors can result from either a steep Balmer break followed by a flattening or a continuously rising power-law. Figure 6 illustrates this degeneracy, showing examples of both types of SEDs across a range of rest-frame $[0.3\text{--}0.9 \mu\text{m}]$ colors.

The left panel of Figure 6 shows LRDs with pronounced curvature, following the trend between $[0.3\text{--}0.9 \mu\text{m}]$ color and curvature strength ($a \cdot \log \lambda^2$; see color-coding in Figure 4). The reddest, highest-curvature sources exhibit the most extreme Balmer breaks: their SEDs rise steeply in the optical and then flatten sharply toward the NIR. Moving toward bluer LRDs, the break becomes less pronounced, the optical slope shallower, and the flattening shifts to longer wavelengths. A simple interpretation in the context of a two-component model, would be that the relative luminosity of the break-dominated component gradually decreases top-to-bottom, effectively hiding the steep slope and pushing the inflection point redward.

The right panel of Figure 6 shows power-law LRDs. While most are blue, a small fraction ($\sim 10\%$) exhibit very red colors ($[0.3\text{--}0.9 \mu\text{m}] > 3$ in Figure 4). These red power-law sources show a range of optical slopes, suggesting variation in the physical conditions shaping the continuum, such as dust attenuation or gas density in BH* models. Notably, the reddest of these LRDs, JADES-GDN-68797 and MACSJ0647.7+7015 (one of the first reported LRDs; Killi et al. 2023), exhibit remarkably similar optical slopes, despite the latter being about 1 mag bluer. This also agrees with the apparent shift in the inflection point from the flat UV to the rising optical continuum in this object, which occurs at longer wavelengths. A similar shift is seen in “Virgil” (yellow) and other bluer LRDs, as discussed in the previous section. We return to this point in § 5.

4.5. Color Dependence of the Emission Line FWHMs

Next, we analyze how the widths of broad emission lines correlate with rest-frame colors. The ubiquitous broad lines observed in LRDs were among the key motivations for their initial interpretation as AGNs. Early black hole mass estimates based on these lines suggested surprisingly high black hole-to-stellar mass ratios (Kocevski et al. 2023a; Harikane et al. 2023; Greene et al. 2024; Maiolino et al. 2023). While recent studies have identified exponential wings in the broad-line profiles, potentially indicating that standard virial mass estimators may not apply (Naidu et al. 2025; Rusakov et al. 2025), it remains important to test whether line width correlates with overall rest-frame color, which, as we have shown, is closely tied to the diversity of LRD SEDs.

The left panel of Figure 7 shows the same rest-frame color-slope diagram as Figure 4, now color-coded by the FWHM of the broad lines, compiled from BLAGNs in the literature as described in § 3.3. We use measurements from NIRSPEC grating observations reported in Kocevski et al. (2023a), Taylor et al. (2024), Juodžbalis et al. (2025), and Hviding et al. (2025), along with individual values from other studies (e.g., Akins et al. 2024a; de Graaff et al. 2025a; Naidu et al. 2025). We also include NIRCAM/WFSS-based estimates from Matthee et al. (2024) and Zhang et al. (2025). For LRDs with NIRSPEC/Prism continuum and $S/N_{UV} > 2$, rest-frame colors are computed directly from the spectra (circles). For lower-S/N sources or those without spectra, we use rest-frame colors derived from best-fit photometric SEDs (squares and stars).

The colormap suggests a positive correlation, with the reddest LRDs showing the highest FWHMs. A color vs. FWHM linear fit yields a statistically significant correlation, albeit with substantial scatter (Pearson $r = 0.33$, $p = 2.7 \times 10^{-3}$; Spearman $\rho = 0.36$, $p = 1.0 \times 10^{-3}$). The median FWHM, binned by rest-frame color as in Figure 5, declines from $2327 \pm 760 \text{ km s}^{-1}$ for $[0.3\text{--}0.9 \mu\text{m}] > 3$, to $2067 \pm 877 \text{ km s}^{-1}$ for $2 < [0.3\text{--}0.9 \mu\text{m}] < 3$, and $1677 \pm 955 \text{ km s}^{-1}$ for $[0.3\text{--}0.9 \mu\text{m}] < 2$. This trend agrees with the results of Greene et al. (2024), who found broader lines in redder LRDs (e.g., $F277W\text{--}F444W > 1.6$) in the UNCOVER field.

Despite this general trend, the scatter is large, and there are notable exceptions. Some blue LRDs exhibit very broad lines, for example, GOODS-N-1001830 from Juodžbalis et al. (2024a) and UNCOVER-38018 from Greene et al. (2024) both show $\text{FWHM} > 4000 \text{ km s}^{-1}$. Conversely, some of the reddest LRDs, such as RUBIES-UDS-16053 (Taylor et al. 2025) and “The Cliff” (de Graaff et al. 2025a), exhibit narrower lines with $\text{FWHM} \lesssim 1500 \text{ km s}^{-1}$.

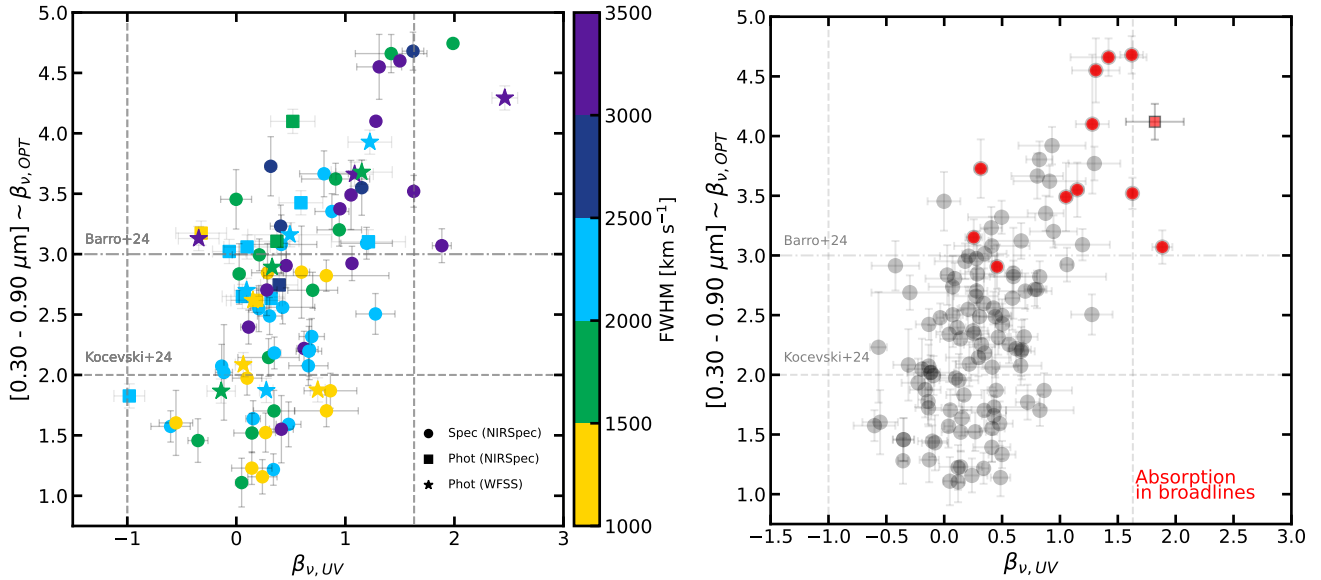


Figure 7. *Left:* Same color-slope diagram as in Figure 4 but color-coded by the FWHM of broad emission lines compiled from the literature (Greene et al. 2024; Kocevski et al. 2023a; Taylor et al. 2024; Juodžbalis et al. 2025; Akins et al. 2024a; de Graaff et al. 2025a; Naidu et al. 2025; Matthee et al. 2024; Zhang et al. 2025). Circles show LRDs with spectroscopic color measurements; squares and stars indicate colors derived from photometric SED fits for sources with lower S/N or no NIRSpec continuum. LRDs with the reddest colors ($[0.3-0.9 \mu\text{m}] > 3.5$ mag) and redder UV slopes tend to have the broadest emission lines. *Right:* Same diagram, now highlighting LRDs with narrow absorptions in their broad emission lines, as compiled from the literature (see text). Red circles mark the LRDs with reported absorption features; the open red square indicates the candidate from Torralba et al. (2025), for which no public spectrum is available, and the classification is based on photometry. Grey dots show other NIRSpec LRDs with no reported absorptions. Absorbers occupy the reddest end of the distribution and exhibit the characteristic strong breaks and optical curvature of this population.

4.6. LRDs with narrow absorption in the broad emission lines

We now examine the subset of LRDs that exhibit narrow absorption features superimposed on their broad Balmer lines. These absorptions exhibit large EWs that exceed expectations from stellar photospheres, pointing instead to very dense gas near the broad-line region (Matthee et al. 2024; D’Eugenio et al. 2025c,a; Torralba et al. 2025). Consequently, their presence has become a key prediction of the BH* scenario, in which the optically thick gas cocoon produces both strong Balmer breaks and broad absorption features (Inayoshi & Maiolino 2024; Ji et al. 2025).

We compile 12 such LRDs with reported absorptions across the six JWST fields, as identified in the literature by Kocevski et al. (2024), Wang et al. (2024b) (RUBIES-EGS-55604, -49140, -42046), Juodžbalis et al. (2024a) (1181-28074; “Rosetta”), Furtak et al. (2023), Ji et al. (2025) (A2744-QSO1), Labbe et al. (2024) (A2744-45924), Wang et al. (2024a) (RUBIES-UDS-BLAGN1), de Graaff et al. (2025a) (RUBIES-UDS-154183; “The Cliff”), Naidu et al. (2025) (MoM-BH*-1), D’Eugenio et al. (2025a) (1286-159717), Taylor et al. (2025) (CAPERS-BH*-1), and Torralba et al. (2025)

(GDN-9771). The last object is included for completeness, though no public spectrum is available, and its properties are inferred from photometry.

The right panel of Figure 7 shows the positions of these broad-line absorbers in the rest-frame color-slope diagram. Nearly all lie at the red end of the distribution, with a mean optical color of $[0.3-0.9 \mu\text{m}] = 3.75 \pm 0.62$ mag. Notably, this includes all three of the extreme BH*-like LRDs with $[0.3-0.9 \mu\text{m}] \gtrsim 4$ from de Graaff et al. (2025a), Naidu et al. (2025), and Taylor et al. (2025). Consistent with their red optical colors, most also show strong Balmer breaks ($\gtrsim 3$ mag) and pronounced optical curvature. These properties weaken toward the bluer end of the distribution: the three absorbers with $[0.3-0.9 \mu\text{m}] < 3.25$ have shallower Balmer breaks ($\lesssim 2$ mag), and one of them, 1286-159717 from D’Eugenio et al. (2025a), has a clear power-law-like SED instead.

This strong correlation with optical color raises the question of whether all LRDs with $[0.3-0.9 \mu\text{m}] \gtrsim 3$ exhibit such absorptions. However, most of these red LRDs are covered only by NIRSpec/PRISM spectroscopy, which lacks the spectral resolution required to detect narrow absorption features (e.g., all LRDs in UNCOVER and COSMOS). Of the 13 spectroscopic LRDs

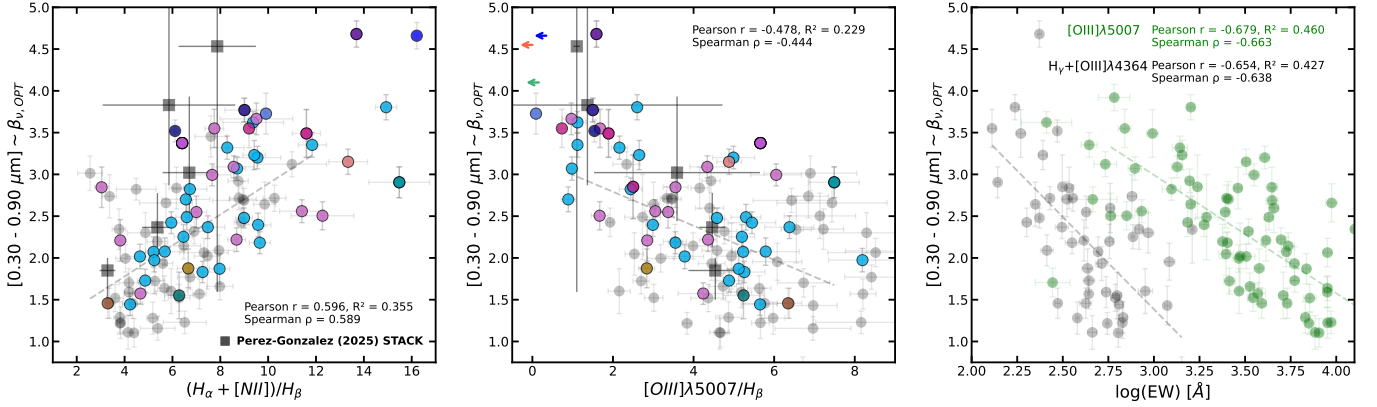


Figure 8. Emission line ratios and equivalent widths for spectroscopic LRDs as a function of [0.3–0.9 μm] color. Only lines with high S/N >5 are included. Colored markers in the first two panels highlight LRDs from the literature, as in Figure 4. Black squares show the same line ratios measured from the stacked spectra in each color bin by Pérez-González (in prep.), as shown in Figure 5. *Left:* The Balmer decrement ($H\alpha/H\beta$) increases with [0.3–0.9 μm] color, peaking in the reddest LRDs. *Center:* The $[OIII]\lambda 5007/H\beta$ ratio declines with [0.3–0.9 μm] color. Bluest LRDs show the highest values, while the reddest, BH*–like LRDs exhibit weak or absent $[OIII]\lambda 5007$. *Right:* The equivalent widths of $[OIII]\lambda 5007$ (green) and $H\gamma + [OIII]\lambda 4364$ (gray) both decline toward redder [0.3–0.9 μm] values, suggesting that narrow emission lines become stronger in bluer LRDs, suggesting a more dominant role of the galaxy host.

with $[0.3\text{--}0.9 \mu\text{m}] \gtrsim 3$ not previously identified as absorbers, only five have higher-resolution grating spectra that cover one or more of the main broad lines (e.g., $H\alpha$, $H\beta$, or He I): RUBIES-UDS-31749, -127928 (faint), RUBIES-EGS-42232, -926125, and JADES-GDN-1181-68797. All five show broad $H\alpha$ emission and are listed in the BLAGN catalogs from Taylor et al. (2024) and Hviding et al. (2025), but none show reported narrow absorption features.

4.7. Color Dependence of Emission-line Ratios

Lastly, we examine the emission-line fluxes and equivalent widths of LRDs as a function of rest-frame [0.3–0.9 μm] color, using line measurements from the DJA/NIRSpec v4.4 release. These line fluxes are derived using a combination of spline fits to the continuum and Gaussian profiles (convolved with the instrumental resolution) for the emission lines (see Valentino et al. 2025 for details). We restrict our analysis to the high-continuum-S/N LRDs discussed throughout this section and consider only emission lines with robust detections ($S/N > 5$) measured in the NIRSpec/PRISM spectra.

Figure 8 shows the trends between key emission-line ratios and [0.3–0.9 μm] color. Colored markers highlight well-studied LRDs from the literature, following the same color scheme as in Figure 4. Black squares indicate the same line ratios measured on stacked spectra, binned by UV-to-optical color, from Pérez-González et al. (in prep.). The left panel shows the (blended) $H\alpha + [NII]$ to $H\beta$ ratio, with high-S/N detections available for nearly 86% of the sample. The remaining sources are mostly at $z > 7$, where $H\alpha$ lies beyond the

NIRSpec/PRISM spectral range. The line ratio shows a clear positive correlation: the reddest LRDs tend to show significantly stronger $H\alpha + [NII]$ emission relative to $H\beta$. This trend is broadly consistent with values derived from the stacked spectra (Pérez-González et al., in prep.) and recent results from de Graaff et al. (2025c). Some discrepancies arise in the reddest bins, where larger uncertainties and the stacking process likely dilute the contribution from the most extreme BH* LRDs, which are rare and therefore underrepresented.

Extreme examples like “The Cliff” and RUBIES-UDS-BLAGN1 lie at the upper right of the diagram, with the highest line ratios. Other prominent BH* LRDs from Naidu et al. (2025) and Taylor et al. (2025) are absent due to the lack of $H\alpha$ coverage at their higher redshifts. The observed Balmer decrements span a broad range ($\sim 2\text{--}20$), with most values exceeding the canonical Balmer decrement of $H\alpha/H\beta = 3.1$ expected for AGN narrow-line regions under Case B recombination (Osterbrock & Ferland 2006). Because LRDs generally exhibit broad Balmer lines, the $H\alpha + [NII]$ to $H\beta$ ratio measured at PRISM resolution largely probes the conditions of the broad-line region (BLR). In contrast, the narrow-line Balmer decrement measured in higher-resolution spectra typically yields much lower ratios, closer to the theoretical value (e.g., Killi et al. 2023; Akins et al. 2024b; D’Eugenio et al. 2025c; Brooks et al. 2025).

The physical origin of the large Balmer decrement in LRDs remains poorly understood. Early interpretations invoking heavy obscuration (e.g., Kocevski et al. 2023a, Greene et al. 2024) are disfavored in light of the BH* models, which predict more complex radiative transfer

effects. In this context, the elevated broad $H\alpha/H\beta$ ratios may be boosted by collisional excitation and resonant scattering in the dense, low-metallicity (and low-extinction) gas cocoon surrounding the accreting black hole (e.g., Chang et al. 2025; Torralba et al. 2025; Yan et al. 2025). Supporting this scenario, the LRDs with the most extreme $H\alpha/H\beta$ ratios are also those that exhibit narrow self-absorption features superimposed on their broad Balmer lines.

The central panel of Figure 8 shows the $[\text{OIII}]\lambda 5007/H\beta$ flux ratio as a function of $[0.3-0.9 \mu\text{m}]$ color. These lines are detected in nearly 90% of the LRD sample. This line ratio exhibits a clear negative trend: redder LRDs exhibit weaker $[\text{OIII}]\lambda 5007$ emission relative to $H\beta$, while the bluer LRDs show elevated $[\text{OIII}]\lambda 5007/H\beta$ ratios. The three BH* candidates (“The Cliff,” MoM-BH*1, and CAPERS-119334) stand out at the top-left of the diagram, with $[\text{OIII}]\lambda 5007/H\beta \ll 1$ due to their strong broad $H\beta$ emission and near-complete absence of $[\text{OIII}]\lambda 5007$. On the opposite end, the bluest LRDs feature some of the highest ratios with “Virgil” (Rinaldi et al. 2025) featuring one of the highest $[\text{OIII}]\lambda 5007/H\beta \sim 6.5$ values. This trend is also supported by stacked spectra (Perez-Gonzalez et al., in prep.) and by de Graaff et al. (2025c), who find similarly low $[\text{OIII}]\lambda 5007/H\beta$ in the reddest LRDs.

At first glance, the observed trend may seem counterintuitive, as classical excitation diagnostics (e.g., the BPT diagram; Baldwin et al. 1981) associate high $[\text{OIII}]\lambda 5007/H\beta$ ratios with AGN activity in low-redshift galaxies. Yet, in LRDs, the reddest and most AGN-dominated systems, marked by broad lines and extreme SEDs, show the lowest $[\text{OIII}]\lambda 5007/H\beta$ ratios. This can be understood if the broad $H\beta$ originates in the BLR, while $[\text{OIII}]\lambda 5007$, typically emitted from the host galaxy or narrow-line region (NLR), is weak or absent. As $[0.3-0.9 \mu\text{m}]$ color becomes bluer, $[\text{OIII}]\lambda 5007$ emission strengthens, likely tracing a nascent NLR or the galaxy host beyond the BH* cocoon. In some LRD with high-resolution NIRSPEC spectra, where broad and narrow components can be separated, the narrow-line ratio reaches $([\text{OIII}]\lambda 5007/H\beta)_{\text{narrow}} \sim 10$, compared to the unresolved PRISM ratio of $[\text{OIII}]\lambda 5007/H\beta \sim 2$ (e.g., D’Eugenio et al. 2025d; Jones et al. 2025). In even bluer LRDs, the broad $H\beta$ component fades relative to the narrow, often becoming indistinguishable (D’Eugenio et al. 2025c; Juodžbalis et al. 2024b; Akins et al. 2024b; Rinaldi et al. 2025). As a result, PRISM-based ratios more closely reflect the intrinsic narrow-line value, similar to those in normal galaxies (Roberts-Borsani et al. 2024; Backhaus et al. 2024), supporting

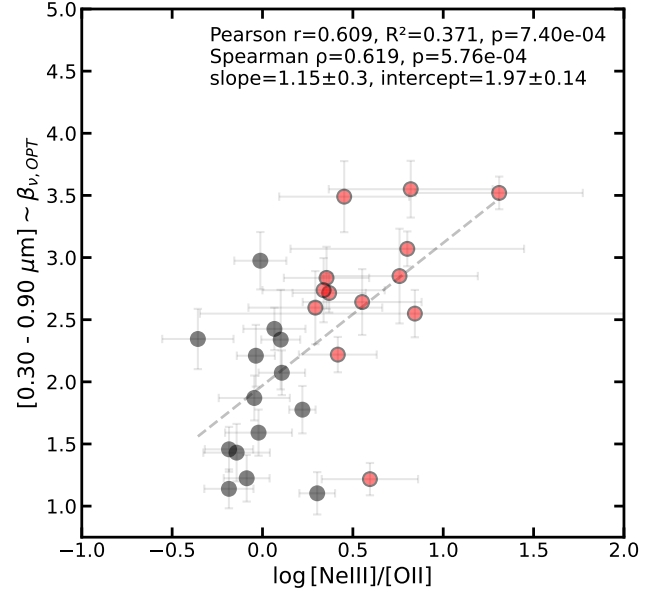


Figure 9. $[\text{NeIII}]/[\text{OII}]$ line ratio as a function of rest-frame $[0.3-0.9 \mu\text{m}]$ color for spectroscopic LRDs. Only 12% of sources have both lines detected at $S/N > 5$ (gray), while an additional 10% have high- S/N $[\text{NeIII}]$ and lower- S/N ($2 < S/N < 5$) $[\text{OII}]$ detections (red). These latter sources are predominantly redder in $[0.3-0.9 \mu\text{m}]$ and drive an overall positive correlation between color and line ratio. Since both lines are narrow and likely originate in the host galaxy, the trend may reflect changing ionization conditions or metallicity in the galaxy population.

a scenario in which narrow-line emission in blue LRDs arises primarily from the host.

To further test whether narrow emission lines arise from the host galaxy while the optical continuum is AGN-dominated, we examine the correlation between equivalent width (EW) and $[0.3-0.9 \mu\text{m}]$ color for the most prominent narrow lines. The right panel of Figure 8 shows the EW of $[\text{OIII}]\lambda 5007$ and the of blended $H\gamma + [\text{OIII}]\lambda 4364$ the latter serving as a proxy for the complex of lines near the Balmer-break ($[\text{OII}]$, $[\text{NeIII}]$, $H\delta$) commonly seen in high-EW galaxies. Among these, $H\gamma + [\text{OIII}]\lambda 4364$ is typically the strongest and most reliably detected, with $\sim 45\%$ of LRDs showing $S/N > 5$ in this feature, compared to 20%, 18%, and 1% for $[\text{OIII}]\lambda 5007$, $[\text{NeIII}]$, and $[\text{OII}]$, respectively. Both EWs show a clear anti-correlation with $[0.3-0.9 \mu\text{m}]$ color: bluer LRDs exhibit stronger narrow-line emission, while redder LRDs show much weaker or undetected lines. This supports the picture that narrow-line features become more prominent toward bluer LRDs, where the host galaxy likely contributes more to the spectrum.

We caution that $H\gamma + [\text{OIII}]\lambda 4364$ may not be purely narrow, especially in the reddest LRDs where broad $H\gamma$

Table 2. Properties of LRDs with NIRSpect PRISM spectra

DJA Name	RA	Dec	z_{spec}	$\beta_{\nu, \text{UV}}$	[0.3–0.9 μm]	$\log(M_{\star}/M_{\odot})$	$A_{V, \text{gal}}$	$A_{V, \text{BH}}$
rubies-egs61-v4-69475	214.949188	52.964137	5.620	0.41 ± 0.23	2.06 ± 0.17	7.45 ± 0.16	0.15 ± 0.06	0.00 ± 0.03
ceers-ddt-v4-1768	214.925759	52.945659	5.088	0.50 ± 0.29	3.32 ± 0.14	7.14 ± 0.26	0.20 ± 0.05	0.00 ± 0.07
rubies-egs61-v4-61496	214.972440	52.962191	5.084	0.70 ± 0.23	2.70 ± 0.15	7.89 ± 0.81	0.25 ± 0.14	1.50 ± 0.76
capers-egs53-v4-7761	214.840034	52.860648	3.859	0.22 ± 0.12	2.62 ± 0.19	7.92 ± 0.35	0.26 ± 0.06	0.00 ± 0.20
capers-egs49-v4-8752	214.876137	52.880826	8.357	0.60 ± 0.07	2.85 ± 0.38	8.77 ± 0.15	0.32 ± 0.04	1.24 ± 0.39
rubies-egs61-v4-55604	214.983030	52.956002	6.989	1.05 ± 0.05	3.49 ± 0.29	9.62 ± 0.21	0.59 ± 0.07	1.50 ± 0.25
capers-egs47-v4-9244	214.985675	52.956230	5.200	0.12 ± 0.05	1.64 ± 0.17	7.58 ± 0.04	0.09 ± 0.02	0.08 ± 0.20
capers-egs53-v4-10108	214.797532	52.818752	6.623	0.21 ± 0.09	1.98 ± 0.19	7.87 ± 0.20	0.17 ± 0.04	0.13 ± 0.31

NOTE— This table is available in its entirety at <https://github.com/guillermobc/Barro25>.

emission can dominate. Still, high-resolution NIRSpect spectra suggest that the narrow $\text{H}\gamma$ component becomes more prominent in bluer LRDs (e.g., Akins et al. 2024b; Juodžbalis et al. 2024b; Rinaldi et al. 2025), while the broad component dominates over the narrow in redder systems (e.g., D’Eugenio et al. 2025c; Jones et al. 2025; Torralba et al. 2025) similarly to $\text{H}\beta$.

While other narrow lines in the Balmer-break complex are less frequently detected at high S/N, they still provide valuable diagnostics. In particular, the $[\text{NeIII}]/[\text{OII}]$ ratio is a known AGN indicator at low redshift, where elevated values are linked to harder ionizing spectra (e.g., Trump et al. 2023; Backhaus et al. 2022, 2024). Figure 9 shows $[\text{NeIII}]/[\text{OII}]$ as a function of [0.3–0.9 μm] color. We find a positive correlation, with redder LRDs tending to show stronger $[\text{NeIII}]$ relative to $[\text{OII}]$. However, only about 12% of LRDs have S/N>5 detections in both lines (grey circles), with a median color of [0.3–0.9 μm] ~ 1.95 . Another 10% (red circles) show weaker $[\text{OII}]$ ($2 < \text{S/N} < 5$) but measurable $[\text{NeIII}]$, with a redder median color of [0.3–0.9 μm] ~ 2.88 , driving the overall trend.

Although elevated $[\text{NeIII}]/[\text{OII}]$ typically signals AGN photoionization, if narrow lines in LRDs primarily trace the host galaxy, the trend could instead reflect changing host conditions, such as higher dust content or ionization parameter, in redder systems. We note, however, that $[\text{OII}]$ is difficult to measure in red LRDs, as it lies close to the Balmer break where the continuum drops steeply, making reliable fits challenging at PRISM resolution.

The UV emission lines in LRDs are generally faint, with few detections of classical AGN tracers such as $\text{CIII}]$, CIV , or MgII above S/N >5. The exception is $\text{Ly}\alpha$, detected in $\sim 20\%$ of the sample. While $\text{Ly}\alpha$ equivalent widths show no clear trend with color, detections are concentrated in bluer LRDs, with a median [0.3–0.9 μm] $\sim 2.0_{-0.7}^{+0.6}$. Lowering the detection threshold to S/N >2 boosts the $\text{CIII}]$ detection rate to $\sim 22\%$, consistent with it being the brightest UV line after $\text{Ly}\alpha$; CIV and MgII remain below 5%. Like $\text{Ly}\alpha$, $\text{CIII}]$ de-

tections span a wide color range but are slightly redder on average, with [0.3–0.9 μm] $\sim 2.4_{-0.6}^{+0.7}$, consistent with previous reports of $\text{CIII}]$ in some of the reddest LRDs (e.g., Labbe et al. 2024; D’Eugenio et al. 2025c; Torralba et al. 2025).

Although $\text{CIII}]$ is a common AGN tracer at low redshift, its interpretation in LRDs is less clear. Hard radiation fields in high-redshift star-forming galaxies can also power strong $\text{CIII}]$ emission, complicating its association with BH^* activity (e.g., Nakajima et al. 2018). In fact, recent blind surveys for $\text{CIII}]$ emitters and other high-EW UV-line sources at $z > 4$ find that these systems tend to have much bluer [0.3–0.9 μm] colors (< 1), with only $\sim 10\%$ overlap with the LRD population (Arevalo-Gonzalez in prep.; Davis in prep.), suggesting they trace largely distinct populations.

5. A SEMI-EMPIRICAL MODEL FOR LRD SEDS: FROM “THE CLIFF” TO “VIRGIL”

5.1. A Two-Component model: galaxy plus BH^*

Initial efforts to model the peculiar blue UV and red optical SEDs of LRDs focused on multi-component fits combining stellar and AGN templates. These aimed to avoid the extreme stellar masses or non-standard attenuation laws required by single-component models (Kocevski et al. 2023a; Barro et al. 2024a; Wang et al. 2024a; Labbe et al. 2024). A key challenge in these models is reproducing the sharp inflection between the blue UV continuum and the red optical slope, which often aligns precisely with the Balmer limit (Setton et al. 2024). The recent confirmation of several LRDs with extreme Balmer breaks (> 3 mag), inconsistent with any known stellar population (de Graaff et al. 2024; Naidu et al. 2025; Taylor et al. 2025), has prompted a shift toward models involving dense gas envelopes around accreting black holes. In these so-called BH^* scenarios, emission from hot ($T \sim 10^4$ K), dense gas, analogous to stellar atmospheres, can naturally produce Balmer breaks as strong or stronger than those from evolved stellar populations (Inayoshi & Maiolino 2024). While early imple-

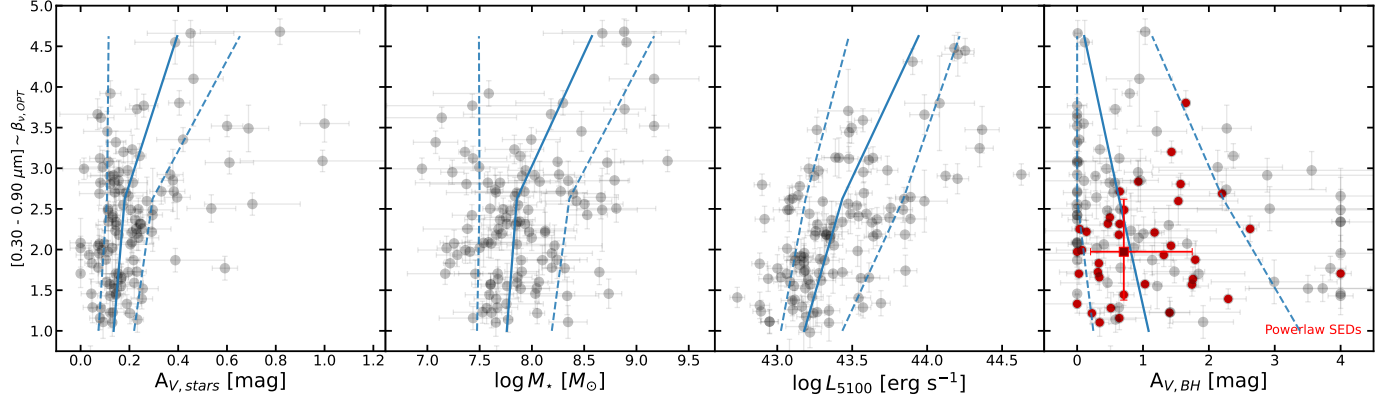


Figure 10. Best-fit parameters of the two-component (galaxy plus BH^{*}) model as a function of rest-frame $[0.3–0.9 \mu\text{m}]$ color for LRDs with high-S/N NIRSpec/PRISM spectra. The panels show stellar attenuation ($A_{V,*}$), stellar mass, BH^{*} luminosity (L_{5100}), and BH^{*} attenuation ($A_{V,BH}$). Stellar attenuation and mass remain approximately constant over $[0.3–0.9 \mu\text{m}] \sim 1–3$, but increase toward the reddest LRDs. Similarly, BH^{*} luminosity increases with color, while $A_{V,BH}$ decreases, reaching its lowest values in the reddest LRDs. Red symbols highlight LRDs with power-law SEDs, which show systematically higher $A_{V,BH}$.

mentations cannot yet reproduce the full rest-optical to NIR spectrum probed by MIRI (de Graaff et al. 2025a; Taylor et al. 2025), they provide a plausible mechanism for the sharp SED turnover at the Balmer limit, since the red BH^{*} component contributes little flux blueward of the break.

Building on this framework, Naidu et al. (2025) modeled the SED of the LRD from Furtak et al. (2024) (see also Ji et al. 2025; D’Eugenio et al. 2025c) using a two-component model combining a UV-bright stellar population with a BH^{*} component dominating the optical continuum. This success suggests the model could be extended to the broader LRD population. However, to do so, it must account for: (1) the wide range in UV-to-optical colors, (2) the diversity in spectral shapes, including strong curvature and power-law types, and (3) the systematic shift in the SED inflection point from the Balmer limit to longer wavelengths in progressively bluer LRDs, as discussed in the previous section.

To address these constraints, we adopt a semi-empirical model combining a galaxy and a BH^{*} component. Instead of a complex parametric approach using photoionization codes like CLOUDY (Ferland et al. 1998), we use a simplified method where the BH^{*} component is modeled using the observed continuum of the extreme LRD “The Cliff” (de Graaff et al. 2025a). A similar strategy was recently adopted by de Graaff et al. (2025c) and Umeda et al. (2025), who approximate the BH^{*} SED with a blackbody. Here, we construct the BH^{*} template by fitting a low-order polynomial to the emission-line-free regions of the “The Cliff” spectrum, capturing its shape from the Balmer break to $\sim 1 \mu\text{m}$ rest-frame. We assume no UV emission from the BH^{*} component (see § 6 for further discussion). Dust attenuation is applied using an SMC law (Pei 1992), with A_V as the only

free parameter modifying the BH^{*} shape. Even modest attenuation can transform the intrinsic curvature of the BH^{*} template into a redder optical continuum that more closely resembles a power law. Varying both the reddening and relative luminosity of the BH^{*} component naturally shifts the SED inflection point to longer wavelengths. Our model does not include an additional IR component to account for potential dust emission from the BH^{*}, as in Barro et al. (2024b), since the current spectra do not probe the rest-frame NIR ($\lambda \sim 1–3 \mu\text{m}$). Incorporating MIRI data would be essential to assess this contribution and test for warm dust associated with the BH^{*} component.

The stellar component is modeled using *Prospector* (Leja et al. 2019), following the same approach as the two-component models in Pérez-González et al. (2023a) and Barro et al. (2024b), with a τ -model star formation history and a reduced set of free parameters: age, τ , stellar mass, and A_V , assuming fixed sub-solar metallicity. Best-fit properties for the 118 LRDs with high-S/N continuum detections are listed in Table 2.

5.2. Interpreting LRD Diversity Through the Two-Component Model

Our qualitative expectations are confirmed by the distribution of best-fit parameters as a function of rest-frame color across the LRD population. Dividing the sample into three UV-to-optical color bins, $[0.3–0.9 \mu\text{m}] > 3$, $2 < [0.3–0.9 \mu\text{m}] < 3$, and $[0.3–0.9 \mu\text{m}] < 2$, we find that the median stellar attenuation decreases steadily from $A_V = 0.39^{+0.26}_{-0.24}$ in the reddest bin to $0.18^{+0.16}_{-0.10}$ and $0.14^{+0.08}_{-0.10}$ in the intermediate and bluest bins, respectively. Similarly, the stellar mass declines from $\log M_*/M_\odot = 8.57^{+0.60}_{-1.14}$ to $7.85^{+0.49}_{-0.36}$ and $7.76^{+0.42}_{-0.29}$. In contrast, the attenuation of the BH^{*} component in-

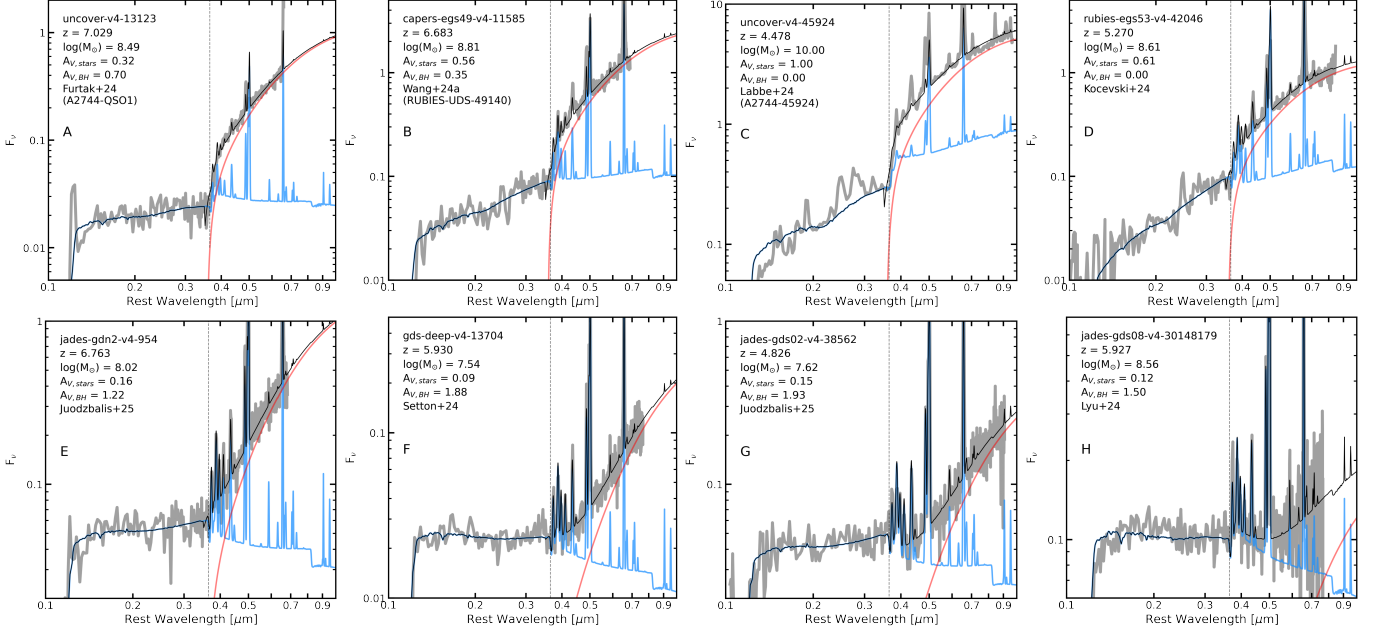


Figure 11. Individual spectra (gray) for representative LRDS spanning the full range of $[0.3\text{--}0.9\ \mu\text{m}]$ colors and SED shapes, from strong curvature to power-law-like continua. Each panel also shows the best-fit two-component model (black), with the galaxy and BH* components plotted separately in blue and red. The dashed vertical line marks the Balmer limit ($H\infty$). Best-fit stellar mass and dust attenuations for both components are indicated. *Top:* Redder LRDS with prominent Balmer breaks and strong optical curvature are best-fit with low BH* attenuation ($A_{V,BH}$), but typically higher stellar attenuation ($A_{V,stars}$) and stellar mass. *Bottom:* Progressively bluer, power-law-like LRDS are best-fit with lower stellar attenuation and mass, but higher BH* attenuation and lower BH* luminosity. This combination shifts the crossover point between galaxy and BH* components to longer wavelengths, shifting the inflection between the flat UV and steep optical continuum (see Figure 12).

increases across the same bins, from $A_{V,BH} = 0.10^{+1.00}_{-0.10}$ to $0.63^{+1.58}_{-0.63}$ and $1.05^{+2.23}_{-0.87}$. Meanwhile, the BH* luminosity declines from $\log(\nu L_\nu)[5100] \equiv \log(L_{5100}[\text{erg s}^{-1}]) = 43.93^{+0.45}_{-0.39}$ to $43.43^{+0.48}_{-0.15}$ and $43.18^{+0.33}_{-0.23}$. These trends suggest that redder LRDS are powered by more luminous, less obscured BH* components embedded in more attenuated stellar hosts, while bluer LRDS tend to host fainter, more obscured BH* components and nearly dust-free galaxies.

Figure 10 illustrates these trends for the full parameter distributions. For the stellar host properties, both A_V and stellar mass remain nearly constant across the bulk of the population ($[0.3\text{--}0.9\ \mu\text{m}] \sim 1\text{--}3$), and then increase toward the reddest, strong-curvature LRDS, accompanied by a larger scatter and uncertainties that reflect the difficulty of constraining the galaxy component when the UV continuum is weak and increasingly dominated by the BH* contribution.

The BH* parameters show a more continuous variation with color. Both the BH* luminosity and $A_{V,BH}$ evolve smoothly across the full $[0.3\text{--}0.9\ \mu\text{m}]$ range, but with substantially larger scatter than the stellar properties. In particular, $A_{V,BH}$ spans a wide range ($A_V \sim 0\text{--}4$) and exhibits large uncertainties at high attenuation, reflecting the increasing difficulty of con-

straining the BH* component as it becomes fainter relative to the galaxy in the composite SED. We also highlight LRDS with power-law SEDs (red circles), which preferentially show higher median $A_{V,BH} \sim 0.8$, consistent with the attenuation required to reproduce their steep optical continua.

Figure 11 shows the best-fit SEDs for representative LRDS with NIRSPEC/PRISM spectra and high continuum S/N. The top row presents the reddest LRDS, characterized by prominent Balmer breaks and strong curvature. Our model reproduces the SED of the [Furtak et al. \(2023\)](#) LRD with a similar configuration to that in [Naidu et al. \(2025\)](#): a minimally attenuated, low-mass stellar component dominating the UV, and an unreddened BH* continuum dominating the optical. The model also fits other red LRDS with strong but less extreme breaks, such as those in [Labbe et al. \(2024\)](#) and [Wang et al. \(2024a\)](#), with slightly higher BH* attenuation ($A_{V,BH} \lesssim 0.6$ mag) and more reddened stellar components, needed to reproduce their red UV slopes. A key reason this model outperforms previous multi-component fits is that the BH* SED features an abrupt drop blueward of the Balmer break, allowing the composite SED to match the sharp inflections observed in these sources. Standard reddened AGN templates tend

to produce smoother transitions that cannot reproduce the observed break amplitude (e.g., Ma et al. 2025).

The bottom row shows progressively bluer LRDs, with decreasing $[0.3\text{--}0.9\ \mu\text{m}]$ colors and power-law-like SEDs. As discussed above, these objects typically have more attenuated and lower-luminosity BH* components, along with nearly dust-free stellar hosts. The model reproduces this sequence by increasing $A_{V,\text{BH}}$ to $\sim 1\text{--}2$ mag while keeping $A_{V,\text{stars}} \sim 0.2$ mag, consistent with their flat UV slopes ($\beta_{\nu,\text{UV}} \sim 0$). Although the power-law shape extends out to $\lambda \sim 1\ \mu\text{m}$, the model predicts a flattening in the rest-frame NIR, which should be testable with MIRI photometry.

Overall, the two-component model successfully fits LRDs across the full range of $[0.3\text{--}0.9\ \mu\text{m}]$ colors and SED types, suggesting that the observed diversity is primarily driven by variations in the BH*-to-galaxy luminosity ratio ($L_{\text{BH}^*}/L_{\text{gal}}$), together with increasing obscuration of the BH* component. As $L_{\text{BH}^*}/L_{\text{gal}}$ declines toward bluer colors, the crossover between the stellar (blue) and BH* (red) continua shifts to longer wavelengths, from $\sim 0.4\ \mu\text{m}$ to $\sim 0.7\ \mu\text{m}$, delaying the onset of the steep optical rise.

To quantify this behavior, Figure 12 shows the wavelength at which the luminosities of the two components are equal, $L_{\text{BH}^*}/L_{\text{gal}} = 1$, denoted as $\lambda_{\text{intersect}}$. While this crossover does not correspond exactly to the inflection point of the composite SED, the steep slope of the BH* continuum ensures that the turnover typically occurs slightly blueward of $\lambda_{\text{intersect}}$. The top y-axis also reports the luminosity ratio $L_{\text{BH}^*}/L_{\text{gal}}$ at $5100\ \text{\AA}$, which provides a measure of the relative normalization of the two components and closely tracks $\lambda_{\text{intersect}}$. We find a clear correlation with color: for the reddest LRDs ($[0.3\text{--}0.9\ \mu\text{m}] \gtrsim 3$), $\lambda_{\text{intersect}}$ lies near the Balmer limit, consistent with Setton et al. (2024). As $[0.3\text{--}0.9\ \mu\text{m}]$ decreases and $L_{\text{BH}^*}/L_{\text{gal}}(5100)$ declines, $\lambda_{\text{intersect}}$ shifts progressively redward, often approaching $[\text{OIII}]\lambda 5007$ or longer wavelengths. Red and blue symbols mark the LRDs shown in Figure 11, illustrating the continuous decline with color. For the bluer LRDs (letters E through H), $L_{\text{BH}^*}/L_{\text{gal}}(5100)$ decreases from ~ 3 to ~ 0.25 , indicating that the BH* becomes subdominant at $5100\ \text{\AA}$. The bluest example, JADES-30148179, exhibits the longest-wavelength crossover and one of the shallowest optical slopes. First reported by Lyu et al. (2024) as a MIRI-selected AGN, this source, like ‘‘Virgil’’ (Iani et al. 2024), exemplifies blue LRDs in which the steepening of the optical continuum becomes apparent only redward of $\text{H}\alpha$, as traced by MIRI photometry.

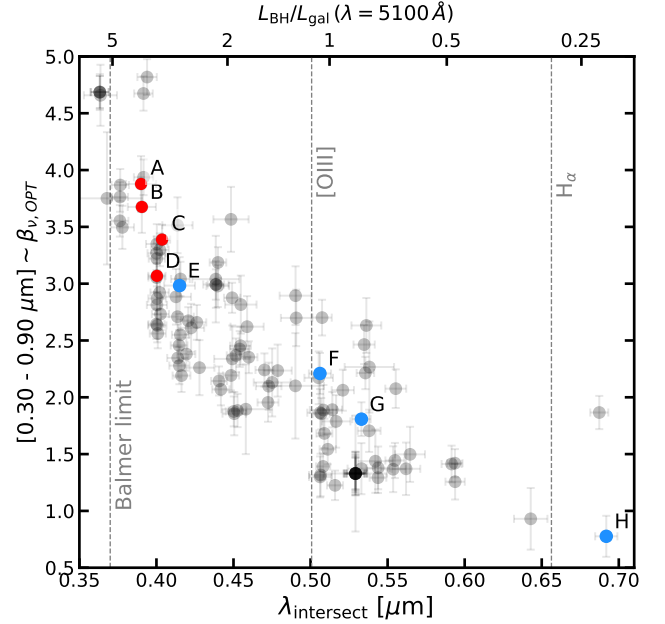


Figure 12. Wavelength at which the BH* and galaxy components have equal luminosity ($L_{\text{BH}^*}/L_{\text{gal}} = 1$), $\lambda_{\text{intersect}}$, as a function of rest-frame $[0.3\text{--}0.9\ \mu\text{m}]$ color for spectroscopic LRDs. This crossover serves as a proxy for the SED inflection, marking the transition from flat UV continua to steep optical slopes. Letters and colors correspond to the LRDs shown in Figure 11, illustrating the shift from inflections near $\text{H}\infty$ in redder LRDs to progressively longer wavelengths in bluer systems as $[0.3\text{--}0.9\ \mu\text{m}]$ decreases.

6. DISCUSSION: TOWARD A UNIFIED VIEW OF THE LRD POPULATION

The semi-empirical two-component model discussed in § 5, in which the rest-frame UV continuum is dominated by stellar emission and the optical by a BH*, provides a useful framework for interpreting the diversity in color and SED shapes of LRD SEDs. Combined with the rest-frame color-slope diagram (Figure 4), it serves as a diagnostic tool for exploring how variations in BH and host galaxy properties shape the observed continuum, and potentially tracing evolutionary paths within the LRD population. These ideas are illustrated schematically in Figure 13.

As discussed throughout this work, three key trends emerge in the color-slope diagram when moving from the reddest to the bluest LRDs: (1) The reddest $\sim 20\%$ of LRDs ($[0.3\text{--}0.9\ \mu\text{m}] \gtrsim 3$) exhibit significantly redder UV slopes, while the majority of the population shows uniformly blue UV slopes with $\beta_{\nu,\text{UV}} \sim 0.3$; (2) the optical continuum shape evolves from strong curvature with Balmer breaks and absorption features to smoother, power-law-like shapes; (3) the FWHM of broad Balmer lines become progressively narrower, while narrow metal

lines grow stronger and more prominent in the bluest LRDs.

A simple schematic picture (downward arrows in Figure 13) is that the spread in $[0.3\text{--}0.9\ \mu\text{m}]$ color reflects variations in the relative luminosity of the BH*–to–host ($L_{\text{BH}^*}/L_{\text{gal}}$). The reddest LRDs are dominated by luminous BH* components, while the bluest ones are increasingly galaxy-dominated, not just in the UV but also into the optical (up to $\sim 5100\ \text{\AA}$), and show stronger narrow lines. As $L_{\text{BH}^*}/L_{\text{gal}}$ declines (due to declining BH* luminosity and/or increased attenuation), the SED inflection point shifts to longer wavelengths, reducing the curvature of the optical continuum and yielding more power-law-like SEDs.

6.1. What is the Origin of the Red UV Continuum?

While this picture explains the majority of LRDs with $[0.3\text{--}0.9\ \mu\text{m}] < 3$, it raises questions for the reddest ones. What causes their red UV slopes? In our default two-component model, the galaxy dominates the UV (Scenario 1: BH* is UV-opaque), so red UV slopes require higher stellar attenuation and masses ($A_V \sim 0.3\text{--}0.5$, $\log M_* \sim 8\text{--}9$), in contrast to the uniformly lower values observed in most LRDs ($A_V \sim 0.15$, $\log M_* \sim 7.5\text{--}8$). At face value, the higher stellar masses inferred for the reddest LRDs would be consistent with their larger inferred black hole masses, suggested by both higher luminosities and broader Balmer lines, and could help alleviate the tension with the large $M_{\text{BH}}/M_* \sim 0.01\text{--}0.1$ ratios in LRDs relative to local relations (e.g., Kocevski et al. 2023a, 2024; Maiolino et al. 2023; Juodžbalis et al. 2025; Jones et al. 2025).

However, the preference for dustier hosts is unexpected in the context of dense, dust-poor gas envelopes favored in BH* models for the reddest LRDs. Moreover, the unusual SED of LRDs and the presence of broad wings in their Balmer lines call into question standard bolometric corrections (Greene et al. 2025) and virial linewidth calibrations (Rusakov et al. 2025; Kokorev et al. 2025), potentially lowering inferred M_{BH} by up to an order of magnitude depending on the accretion rates (D’Eugenio et al. 2025d; Torralba et al. 2025). Interpreted strictly within Scenario 1, the observed trends would imply an evolutionary sequence from bluer to redder LRDs, with both host galaxies and black holes growing in mass over time.

An alternative interpretation (Scenario 2: BH* is UV-transparent) is that the BH* component shows a faint, heavily reddened UV continuum. Although dense gas envelopes are generally expected to suppress emission blueward of the Balmer break, certain combinations of gas density and geometry may allow a small fraction of

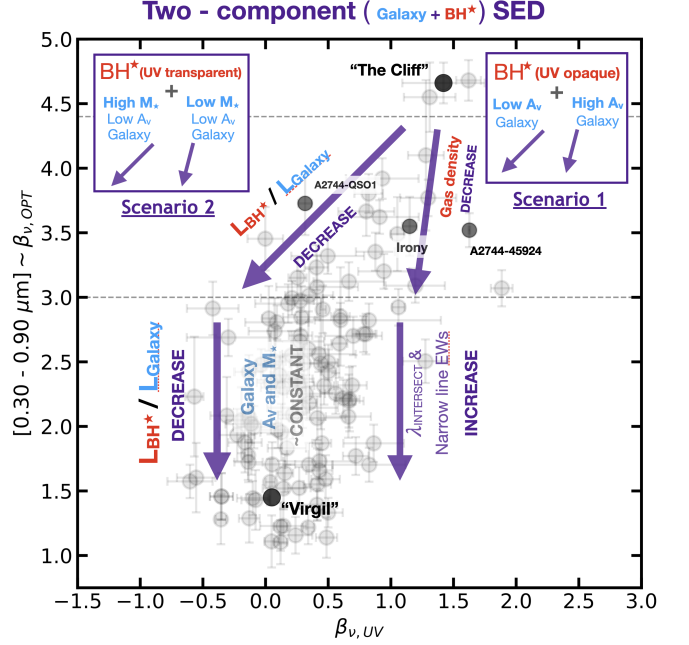


Figure 13. Schematic diagram of two scenarios for interpreting trends in the LRD color–slope diagram based on the two-component galaxy (blue) plus BH* (red) model. In scenario 1 the BH* component never contributes to the UV (opaque). The UV slopes at the red end depend on the dust attenuation of the host. In scenario 2, the BH* exhibits some reddened UV emission at lower gas densities. This UV emission, combined with blue galaxy hosts of different luminosities, can explain the observed range in β_{UV} . Labeled black points mark representative LRDs at key positions in the diagram. Overall, the large observed spread in $[0.3\text{--}0.9\ \mu\text{m}]$ colors among LRDs is primarily driven by variations in the BH*–to–galaxy luminosity ratio, attenuation, and the presence or absence of UV emission from the BH*.

reddened UV light to escape (e.g., Inayoshi & Maiolino 2024; de Graaff et al. 2025a; Naidu et al. 2025). In this case, red UV slopes could arise naturally from the BH* itself, without invoking dusty host galaxies. In bluer LRDs, any such BH* UV emission would be hidden by the brighter galaxy UV continuum.

Within this scenario, shifts toward bluer $[0.3\text{--}0.9\ \mu\text{m}]$ colors could occur through two channels: (1) decreasing $L_{\text{BH}^*}/L_{\text{galaxy}}$ as the host becomes more luminous, or (2) declining gas density or covering fraction, increasing the UV continuum from the BH*. Together, these effects can explain the wide range of UV slopes observed at similar $[0.3\text{--}0.9\ \mu\text{m}]$ colors. For example, A2744-45924 and A2744-QSO1 both have $[0.3\text{--}0.9\ \mu\text{m}] \sim 3.5$ but very different UV slopes ($\beta_{\nu,\text{UV}} \sim 1.5$ and ~ 0 ; A and C in Figure 9). A2744-45924 may represent a more transparent BH* with AGN-dominated UV emission (Labbe et al. 2024), whereas A2744-QSO1 resembles a “Cliff”-like system dominated in the UV by

a bright, dust-free stellar host (Naidu et al. 2025). Other LRDs with similar colors but intermediate slopes (e.g., “Irony” or the Balmer absorbers in Kocevski et al. 2024 and Wang et al. 2024b) likely reflect varying combinations of BH* UV opacity and BH-to-galaxy luminosity ratios.

In this second scenario, the reddest LRDs do not require highly attenuated hosts and may instead have lower stellar masses, as indicated by their sub-dominant UV continua. This would imply an evolutionary sequence opposite to that in Scenario 1, with stellar mass increasing from red to blue LRDs. Under this interpretation, the reddest LRDs could correspond to an early phase of rapid, possibly super-Eddington black hole growth in relatively small galaxies. As LRDs evolve toward bluer [0.3–0.9 μm] colors, their host galaxies would grow more massive while the BH* component fades, either by exiting a high accretion phase or by dispersing the dense gas cocoon. A potential challenge to this picture is that black hole masses would need to remain similar or increase toward bluer LRDs, which appears at odds with their lower luminosities and narrower line widths. However, given the uncertainties in interpreting Balmer line profiles in LRDs, a systematic analysis of line shapes across the full population will be essential to robustly test this evolutionary sequence.

6.2. *Is there any Dust in LRDs?*

In the two-component model, the higher incidence of power-law-like optical SEDs among bluer LRDs is attributed to increased attenuation of the BH* component, which is the primary parameter capable of modifying the continuum shape. In more physically motivated BH* models, similar reddening could arise from higher gas densities or opacities, reducing the need to invoke dust explicitly. Distinguishing between these possibilities requires assessing whether independent evidence for dust is present.

Although a higher BH* attenuation in bluer galaxies may seem counterintuitive, it is plausible if these systems host more evolved galaxies with higher metallicities and dust content, leading to stronger local attenuation near the BH*. Consistent with this picture, MIRI observations indicate that bluer LRDs exhibit redder rest-frame near-infrared colors (e.g., 1–3 μm ; Pérez-González et al. 2024; Barro et al. 2024b), suggestive of warm dust emission. In contrast, the reddest LRDs typically show flatter near-infrared SEDs with little evidence for dust re-emission (e.g., de Graaff et al. 2025a; Setton et al. 2025), supporting the view that they are comparatively dust-poor.

The rest-frame [1–3 μm] color provides a sensitive diagnostic of dust emission. Stellar populations and typical obscured AGNs without significant hot dust produce relatively mild colors ([1–3 μm] \sim 0–0.5; Figure 8 of Barro et al. 2024b), and even BH* or blackbody-like photospheric emission would yield similarly flat or negative values. By contrast, the median [1–3 μm] color of MIRI-detected LRDs is closer to \sim 1.5, implying the presence of warm dust emission or, alternatively, a more complex intrinsic continuum shape than captured by simple BH* models.

Overall, the relatively simple semi-empirical model provides an effective framework for a unified scenario in which LRD diversity arises primarily from variations in the relative luminosities of galaxy and BH* components. This involves some evolution in attenuation and possibly UV-opacity of the BH*, superimposed on a relatively homogeneous population of blue, low-mass, low-extinction galaxies with prominent (high-EW) emission lines. Testing these predictions will require further refinement of BH* models to incorporate more realistic radiative transfer and geometric effects, particularly to explain the red UV slopes in the most extreme LRDs. Similarly, a more systematic MIRI follow-up is essential to confirm whether bluer LRDs indeed show more prominent dust re-emission, as suggested by their red rest-NIR colors. In parallel, deeper and higher-resolution spectroscopy will be crucial to assess the impact of line blending on the PRISM pseudo-continuum and to detect faint high-ionization lines that can help disentangle AGN- from star formation-driven emission.

7. SUMMARY

This paper presents a detailed analysis of a large, uniformly selected sample of Little Red Dots (LRDs) across six JWST deep fields. Using an exhaustive color selection, we identify nearly 1000 photometric LRDs, of which 191 have publicly available NIRSpec/PRISM spectra in the Dawn JWST Archive (DJA) compilation. Within this spectroscopic sample, 118 LRDs have high continuum S/N $>$ 2 in the rest-UV, enabling robust measurements of UV slopes and rest-frame UV-to-optical colors. We use this dataset to quantify the prevalence of broad-line AGN features, characterize the continuum SED shapes among LRDs, and explore correlations between color, SED type, emission line widths, line ratios, and the presence of absorption features.

The main observational results are as follows:

- The fraction of broad-line AGNs (BLAGNs) satisfying the LRD photometric selection is high, ranging from \sim 58–92% across different fields. This

fraction increases with a more inclusive selection that extends to bluer optical slopes.

- Among photometric LRDs with NIRSpec grating spectra at $3.5 < z < 6.8$, $\sim 50\%$ to 90% exhibit broad emission lines, depending on the field. These represent lower limits, as nearly all show clear emission lines, and the identification of broad components is limited by depth and sensitivity.
- The overall LRD population spans nearly 4 magnitudes in $[0.3\text{--}0.9 \mu\text{m}]$ rest-frame color, indicating broad diversity in intrinsic properties. Most NIRSpec LRDs have blue UV slopes with a median $\beta_{\nu,UV} = 0.3^{+0.5}_{-0.4}$ and red UV-to-optical colors with median $[0.3\text{--}0.9 \mu\text{m}] = 2.3^{+0.7}_{-0.7}$. However, the reddest 18% ($[0.3\text{--}0.9 \mu\text{m}] \gtrsim 3$) have significantly redder slopes, reaching $\beta_{\nu,UV} = 1.1^{+0.5}_{-0.6}$.
- A similar trend appears in the optical continuum: LRDs with $[0.3\text{--}0.9 \mu\text{m}] \gtrsim 3$ show pronounced SED curvature, with Balmer breaks and flattening toward the NIR. All literature-reported LRDs with strong breaks fall in this regime. In contrast, bluer LRDs typically show power-law-like optical slopes, forming the canonical “V-shaped” SED.
- While curved SEDs dominate at redder colors and power-laws at the blue end, both types exist across the color range. This overlap reveals a degeneracy in UV-to-optical color: distinct SED shapes can yield similar $[0.3\text{--}0.9 \mu\text{m}]$ values. Like the age–dust degeneracy in stellar populations, this suggests the continuum shape reflects varying combinations of BH luminosity, attenuation, and host galaxy contribution.
- Broad Balmer line widths decrease with color: median FWHM values drop from 2327 km s^{-1} in the reddest LRDs to 1677 km s^{-1} for those with $[0.3\text{--}0.9 \mu\text{m}] < 2$.
- Emission-line ratios and equivalent widths also correlate with $[0.3\text{--}0.9 \mu\text{m}]$: the $\text{H}\alpha + [\text{NII}]/\text{H}\beta$ ratio increases with color (reaching ~ 20 in the reddest), while $[\text{OIII}]\lambda 5007/\text{H}\beta$ decreases. BH^* candidates show the lowest values ($\ll 1$), and bluer LRDs reach up to ~ 8 . The equivalent widths of $[\text{OIII}]\lambda 5007$ and $\text{H}\gamma + [\text{OIII}]\lambda 4364$ decline toward redder colors, suggesting narrow-line emission becomes more prominent in bluer LRDs, consistent with increased host galaxy contribution.

We interpret the range in rest-frame colors, SED types, and emission-line properties using a semi-

empirical two-component model combining a galaxy and a BH^* template. Key results from the modeling include:

- The model successfully fits both curved and power-law SEDs. Curved LRDs require luminous, low-attenuation BH^* components and more obscured stellar hosts. Power-law LRDs are best fit with fainter, highly attenuated BH^* components and nearly dust-free galaxies.
- The broad range in $[0.3\text{--}0.9 \mu\text{m}]$ color is primarily driven by the relative luminosity and attenuation of the BH^* and galaxy components.
- The wavelength where the SED transitions from flat UV to steep optical shifts with color: in redder LRDs ($[0.3\text{--}0.9 \mu\text{m}] \gtrsim 3$), the inflection occurs near the Balmer limit; in bluer LRDs, it shifts progressively redward, beyond $[\text{OIII}]\lambda 5007$ and toward $\text{H}\alpha$.

ACKNOWLEDGMENTS

We thank G. Brammer and the Dawn JWST Archive (DJA) for making high-level data products publicly available. DJA is an initiative of the Cosmic Dawn Center, which is funded by the Danish National Research Foundation under grant No. 140. PGP-G acknowledges support from grant PID2022-139567NB-I00 funded by Spanish Ministerio de Ciencia, Innovación y Universidades MCIU/AEI/10.13039/501100011033, FEDER *Una manera de hacer Europa*.

This work is based on observations made with the NASA/ESA/CSA *James Webb Space Telescope*. The data were obtained from the Mikulski Archive for Space Telescopes (MAST) at the Space Telescope Science Institute (STScI), which is operated by the Association of Universities for Research in Astronomy, Inc., under NASA contract NAS 5-03127. These observations are associated with JWST programs GTO-1180, GTO-1181, GTO-1215, GTO-1286, GO-1345, GO-2198, GO-2561, DDT-2750, GO-3073, GO-4106, GO-4233, GO-5224, GO-6585, GO-6838, and DDT-6541.

JSD acknowledges the support of the Royal Society via the award of a Royal Society Research Professorship. This work has made use of the Rainbow Cosmological Surveys Database, which is operated by the Centro de Astrobiología (CAB), CSIC-INTA, partnered with the University of California Observatories at Santa Cruz (UCO/Lick, UCSC). This project has received funding from the European Union’s Horizon 2020 research and innovation programme under the Marie Skłodowska-Curie grant agreement No 101148925.

Software: Astropy (Astropy Collaboration et al. 2022), EAZY (Brammer et al. 2008), GALFIT (Peng

et al. 2002), matplotlib (Hunter 2007), NumPy (van der Walt et al. 2011), PZETA (Pérez-González et al. 2008b), Prospector (Leja et al. 2019 Johnson et al. 2021), Rain-

bow pipeline (Pérez-González et al. 2005, 2008b, Barro et al. 2011), SExtractor (Bertin & Arnouts 1996), Synthesizer (Pérez-González et al. 2005, 2008a)

REFERENCES

- Akins, H. B., Casey, C. M., Lambrides, E., et al. 2024a, arXiv e-prints, arXiv:2406.10341, doi: [10.48550/arXiv.2406.10341](https://doi.org/10.48550/arXiv.2406.10341)
- Akins, H. B., Casey, C. M., Berg, D. A., et al. 2024b, arXiv e-prints, arXiv:2410.00949, doi: [10.48550/arXiv.2410.00949](https://doi.org/10.48550/arXiv.2410.00949)
- Astropy Collaboration, Price-Whelan, A. M., Lim, P. L., et al. 2022, *ApJ*, 935, 167, doi: [10.3847/1538-4357/ac7c74](https://doi.org/10.3847/1538-4357/ac7c74)
- Backhaus, B. E., Trump, J. R., Cleri, N. J., et al. 2022, *ApJ*, 926, 161, doi: [10.3847/1538-4357/ac3919](https://doi.org/10.3847/1538-4357/ac3919)
- Backhaus, B. E., Trump, J. R., Pirzkal, N., et al. 2024, *ApJ*, 962, 195, doi: [10.3847/1538-4357/ad1520](https://doi.org/10.3847/1538-4357/ad1520)
- Baggen, J. F. W., van Dokkum, P., Labbe, I., et al. 2023, arXiv e-prints, arXiv:2305.17162, doi: [10.48550/arXiv.2305.17162](https://doi.org/10.48550/arXiv.2305.17162)
- Baldwin, J. A., Phillips, M. M., & Terlevich, R. 1981, *PASP*, 93, 5, doi: [10.1086/130766](https://doi.org/10.1086/130766)
- Barbary, K., Boone, K., & Deil, C. 2015, sep: v0.3.0, v0.3.0, Zenodo, doi: [10.5281/zenodo.156669](https://doi.org/10.5281/zenodo.156669)
- Barro, G., Pérez-González, P. G., Gallego, J., et al. 2011, *ApJS*, 193, 30, doi: [10.1088/0067-0049/193/2/30](https://doi.org/10.1088/0067-0049/193/2/30)
- Barro, G., Pérez-González, P. G., Kocevski, D. D., et al. 2024a, *ApJ*, 963, 128, doi: [10.3847/1538-4357/ad167e](https://doi.org/10.3847/1538-4357/ad167e)
- Barro, G., Perez-Gonzalez, P. G., Kocevski, D. D., et al. 2024b, arXiv e-prints, arXiv:2412.01887, doi: [10.48550/arXiv.2412.01887](https://doi.org/10.48550/arXiv.2412.01887)
- Begelman, M. C., & Dexter, J. 2025, arXiv e-prints, arXiv:2507.09085, doi: [10.48550/arXiv.2507.09085](https://doi.org/10.48550/arXiv.2507.09085)
- Bertin, E., & Arnouts, S. 1996, *A&AS*, 117, 393
- Bezanson, R., Labbe, I., Whitaker, K. E., et al. 2024, *ApJ*, 974, 92, doi: [10.3847/1538-4357/ad66cf](https://doi.org/10.3847/1538-4357/ad66cf)
- Brammer, G. 2019, Grizli: Grism redshift and line analysis software, Astrophysics Source Code Library, record ascl:1905.001
- . 2023, msaexp: NIRSpec analysis tools, 0.6.17, Zenodo, doi: [10.5281/zenodo.7299500](https://doi.org/10.5281/zenodo.7299500)
- Brammer, G. B., van Dokkum, P. G., & Coppi, P. 2008, *ApJ*, 686, 1503, doi: [10.1086/591786](https://doi.org/10.1086/591786)
- Brooks, M., Simons, R. C., Trump, J. R., et al. 2025, *ApJ*, 986, 177, doi: [10.3847/1538-4357/addac4](https://doi.org/10.3847/1538-4357/addac4)
- Casey, C. M., Akins, H. B., Kokorev, V., et al. 2024, arXiv e-prints, arXiv:2407.05094, doi: [10.48550/arXiv.2407.05094](https://doi.org/10.48550/arXiv.2407.05094)
- Chang, S.-J., Gronke, M., Matthee, J., & Mason, C. 2025, arXiv e-prints, arXiv:2508.08768, doi: [10.48550/arXiv.2508.08768](https://doi.org/10.48550/arXiv.2508.08768)
- Curtis-Lake, E., Cameron, A. J., Bunker, A. J., et al. 2025, arXiv e-prints, arXiv:2510.01033, doi: [10.48550/arXiv.2510.01033](https://doi.org/10.48550/arXiv.2510.01033)
- de Graaff, A., Brammer, G., Weibel, A., et al. 2024, arXiv e-prints, arXiv:2409.05948, doi: [10.48550/arXiv.2409.05948](https://doi.org/10.48550/arXiv.2409.05948)
- de Graaff, A., Rix, H.-W., Naidu, R. P., et al. 2025a, arXiv e-prints, arXiv:2503.16600, doi: [10.48550/arXiv.2503.16600](https://doi.org/10.48550/arXiv.2503.16600)
- de Graaff, A., Setton, D. J., Brammer, G., et al. 2025b, *Nature Astronomy*, 9, 280, doi: [10.1038/s41550-024-02424-3](https://doi.org/10.1038/s41550-024-02424-3)
- de Graaff, A., Hviding, R. E., Naidu, R. P., et al. 2025c, arXiv e-prints, arXiv:2511.21820, doi: [10.48550/arXiv.2511.21820](https://doi.org/10.48550/arXiv.2511.21820)
- D’Eugenio, F., Juodžbalis, I., Ji, X., et al. 2025a, arXiv e-prints, arXiv:2506.14870, doi: [10.48550/arXiv.2506.14870](https://doi.org/10.48550/arXiv.2506.14870)
- D’Eugenio, F., Cameron, A. J., Scholtz, J., et al. 2025b, *ApJS*, 277, 4, doi: [10.3847/1538-4365/ada148](https://doi.org/10.3847/1538-4365/ada148)
- D’Eugenio, F., Maiolino, R., Perna, M., et al. 2025c, arXiv e-prints, arXiv:2503.11752, doi: [10.48550/arXiv.2503.11752](https://doi.org/10.48550/arXiv.2503.11752)
- D’Eugenio, F., Nelson, E., Ji, X., et al. 2025d, arXiv e-prints, arXiv:2510.00101, doi: [10.48550/arXiv.2510.00101](https://doi.org/10.48550/arXiv.2510.00101)
- Eisenstein, D. J., Johnson, B. D., Robertson, B., et al. 2023, arXiv e-prints, arXiv:2310.12340, doi: [10.48550/arXiv.2310.12340](https://doi.org/10.48550/arXiv.2310.12340)
- Ferland, G. J., Korista, K. T., Verner, D. A., et al. 1998, *PASP*, 110, 761, doi: [10.1086/316190](https://doi.org/10.1086/316190)
- Ferruit, P., Jakobsen, P., Giardino, G., et al. 2022, *A&A*, 661, A81, doi: [10.1051/0004-6361/202142673](https://doi.org/10.1051/0004-6361/202142673)
- Finkelstein, S. L., Bagley, M. B., Arrabal Haro, P., et al. 2025, *ApJL*, 983, L4, doi: [10.3847/2041-8213/adbbd3](https://doi.org/10.3847/2041-8213/adbbd3)
- Furtak, L. J., Zitrin, A., Plat, A., et al. 2023, *ApJ*, 952, 142, doi: [10.3847/1538-4357/acdc9d](https://doi.org/10.3847/1538-4357/acdc9d)
- Furtak, L. J., Labbé, I., Zitrin, A., et al. 2024, *Nature*, 628, 57, doi: [10.1038/s41586-024-07184-8](https://doi.org/10.1038/s41586-024-07184-8)
- Greene, J. E., Labbe, I., Goulding, A. D., et al. 2024, *ApJ*, 964, 39, doi: [10.3847/1538-4357/ad1e5f](https://doi.org/10.3847/1538-4357/ad1e5f)

- Greene, J. E., Setton, D. J., Furtak, L. J., et al. 2025, arXiv e-prints, arXiv:2509.05434, doi: [10.48550/arXiv.2509.05434](https://doi.org/10.48550/arXiv.2509.05434)
- Hainline, K. N., Maiolino, R., Juodžbalis, I., et al. 2024, arXiv e-prints, arXiv:2410.00100, doi: [10.48550/arXiv.2410.00100](https://doi.org/10.48550/arXiv.2410.00100)
- Hainline, K. N., Maiolino, R., Juodžbalis, I., et al. 2025, ApJ, 979, 138, doi: [10.3847/1538-4357/ad9920](https://doi.org/10.3847/1538-4357/ad9920)
- Harikane, Y., Zhang, Y., Nakajima, K., et al. 2023, ApJ, 959, 39, doi: [10.3847/1538-4357/ad029e](https://doi.org/10.3847/1538-4357/ad029e)
- Heintz, K. E., Brammer, G. B., Watson, D., et al. 2025, A&A, 693, A60, doi: [10.1051/0004-6361/202450243](https://doi.org/10.1051/0004-6361/202450243)
- Hunter, J. D. 2007, Computing in Science and Engineering, 9, 90, doi: [10.1109/MCSE.2007.55](https://doi.org/10.1109/MCSE.2007.55)
- Hviding, R. E., de Graaff, A., Miller, T. B., et al. 2025, A&A, 702, A57, doi: [10.1051/0004-6361/202555816](https://doi.org/10.1051/0004-6361/202555816)
- Iani, E., Rinaldi, P., Caputi, K. I., et al. 2024, arXiv e-prints, arXiv:2406.18207, doi: [10.48550/arXiv.2406.18207](https://doi.org/10.48550/arXiv.2406.18207)
- Inayoshi, K., & Maiolino, R. 2024, arXiv e-prints, arXiv:2409.07805, doi: [10.48550/arXiv.2409.07805](https://doi.org/10.48550/arXiv.2409.07805)
- Ji, X., Maiolino, R., Übler, H., et al. 2025, arXiv e-prints, arXiv:2501.13082, doi: [10.48550/arXiv.2501.13082](https://doi.org/10.48550/arXiv.2501.13082)
- Johnson, B. D., Leja, J., Conroy, C., & Speagle, J. S. 2021, ApJS, 254, 22, doi: [10.3847/1538-4365/abef67](https://doi.org/10.3847/1538-4365/abef67)
- Jones, G. C., Übler, H., Maiolino, R., et al. 2025, arXiv e-prints, arXiv:2509.20455, doi: [10.48550/arXiv.2509.20455](https://doi.org/10.48550/arXiv.2509.20455)
- Juodžbalis, I., Ji, X., Maiolino, R., et al. 2024a, MNRAS, 535, 853, doi: [10.1093/mnras/stae2367](https://doi.org/10.1093/mnras/stae2367)
- Juodžbalis, I., Maiolino, R., Baker, W. M., et al. 2024b, Nature, 636, 594, doi: [10.1038/s41586-024-08210-5](https://doi.org/10.1038/s41586-024-08210-5)
- . 2025, arXiv e-prints, arXiv:2504.03551, doi: [10.48550/arXiv.2504.03551](https://doi.org/10.48550/arXiv.2504.03551)
- Killi, M., Watson, D., Brammer, G., et al. 2023, arXiv e-prints, arXiv:2312.03065, doi: [10.48550/arXiv.2312.03065](https://doi.org/10.48550/arXiv.2312.03065)
- Kocevski, D. D., Onoue, M., Inayoshi, K., et al. 2023a, arXiv e-prints, arXiv:2302.00012, doi: [10.48550/arXiv.2302.00012](https://doi.org/10.48550/arXiv.2302.00012)
- Kocevski, D. D., Barro, G., McGrath, E. J., et al. 2023b, ApJL, 946, L14, doi: [10.3847/2041-8213/acad00](https://doi.org/10.3847/2041-8213/acad00)
- Kocevski, D. D., Finkelstein, S. L., Barro, G., et al. 2024, arXiv e-prints, arXiv:2404.03576, doi: [10.48550/arXiv.2404.03576](https://doi.org/10.48550/arXiv.2404.03576)
- Kokorev, V., Caputi, K. I., Greene, J. E., et al. 2024a, arXiv e-prints, arXiv:2401.09981, doi: [10.48550/arXiv.2401.09981](https://doi.org/10.48550/arXiv.2401.09981)
- Kokorev, V., Chisholm, J., Endsley, R., et al. 2024b, arXiv e-prints, arXiv:2407.20320, doi: [10.48550/arXiv.2407.20320](https://doi.org/10.48550/arXiv.2407.20320)
- Kokorev, V., Chisholm, J., Naidu, R. P., et al. 2025, arXiv e-prints, arXiv:2511.07515, doi: [10.48550/arXiv.2511.07515](https://doi.org/10.48550/arXiv.2511.07515)
- Kron, R. G. 1980, ApJS, 43, 305, doi: [10.1086/190669](https://doi.org/10.1086/190669)
- Labbé, I., van Dokkum, P., Nelson, E., et al. 2023, Nature, 616, 266, doi: [10.1038/s41586-023-05786-2](https://doi.org/10.1038/s41586-023-05786-2)
- Labbe, I., Greene, J. E., Bezanson, R., et al. 2023, arXiv e-prints, arXiv:2306.07320, doi: [10.48550/arXiv.2306.07320](https://doi.org/10.48550/arXiv.2306.07320)
- Labbe, I., Greene, J. E., Matthee, J., et al. 2024, arXiv e-prints, arXiv:2412.04557, doi: [10.48550/arXiv.2412.04557](https://doi.org/10.48550/arXiv.2412.04557)
- Leja, J., Carnall, A. C., Johnson, B. D., Conroy, C., & Speagle, J. S. 2019, ApJ, 876, 3, doi: [10.3847/1538-4357/ab133c](https://doi.org/10.3847/1538-4357/ab133c)
- Leung, G. C. K., Finkelstein, S. L., Pérez-González, P. G., et al. 2024, arXiv e-prints, arXiv:2411.12005, <https://arxiv.org/abs/2411.12005>
- Lyu, J., Rieke, G. H., & Shi, Y. 2017, ApJ, 835, 257, doi: [10.3847/1538-4357/835/2/257](https://doi.org/10.3847/1538-4357/835/2/257)
- Lyu, J., Alberts, S., Rieke, G. H., et al. 2024, ApJ, 966, 229, doi: [10.3847/1538-4357/ad3643](https://doi.org/10.3847/1538-4357/ad3643)
- Ma, Y., Greene, J. E., Setton, D. J., et al. 2025, ApJ, 981, 191, doi: [10.3847/1538-4357/ada613](https://doi.org/10.3847/1538-4357/ada613)
- Maiolino, R., Scholtz, J., Curtis-Lake, E., et al. 2023, arXiv e-prints, arXiv:2308.01230, doi: [10.48550/arXiv.2308.01230](https://doi.org/10.48550/arXiv.2308.01230)
- Maseda, M. V., de Graaff, A., Franx, M., et al. 2024, A&A, 689, A73, doi: [10.1051/0004-6361/202449914](https://doi.org/10.1051/0004-6361/202449914)
- Matthee, J., Naidu, R. P., Brammer, G., et al. 2024, ApJ, 963, 129, doi: [10.3847/1538-4357/ad2345](https://doi.org/10.3847/1538-4357/ad2345)
- Naidu, R. P., Matthee, J., Katz, H., et al. 2025, arXiv e-prints, arXiv:2503.16596, doi: [10.48550/arXiv.2503.16596](https://doi.org/10.48550/arXiv.2503.16596)
- Nakajima, K., Schaerer, D., Le Fèvre, O., et al. 2018, A&A, 612, A94, doi: [10.1051/0004-6361/201731935](https://doi.org/10.1051/0004-6361/201731935)
- Oke, J. B., & Gunn, J. E. 1983, ApJ, 266, 713, doi: [10.1086/160817](https://doi.org/10.1086/160817)
- Osterbrock, D. E., & Ferland, G. J. 2006, Astrophysics of gaseous nebulae and active galactic nuclei
- Pei, Y. C. 1992, ApJ, 395, 130, doi: [10.1086/171637](https://doi.org/10.1086/171637)
- Peng, C. Y., Ho, L. C., Impey, C. D., & Rix, H.-W. 2002, AJ, 124, 266, doi: [10.1086/340952](https://doi.org/10.1086/340952)
- Pérez-González, P. G., Trujillo, I., Barro, G., et al. 2008a, ApJ, 687, 50, doi: [10.1086/591843](https://doi.org/10.1086/591843)
- Pérez-González, P. G., Rieke, G. H., Egami, E., et al. 2005, ApJ, 630, 82, doi: [10.1086/431894](https://doi.org/10.1086/431894)

- Pérez-González, P. G., Rieke, G. H., Villar, V., et al. 2008b, *ApJ*, 675, 234, doi: [10.1086/523690](https://doi.org/10.1086/523690)
- Pérez-González, P. G., Costantin, L., Langeroodi, D., et al. 2023a, arXiv e-prints, arXiv:2302.02429, doi: [10.48550/arXiv.2302.02429](https://doi.org/10.48550/arXiv.2302.02429)
- Pérez-González, P. G., Barro, G., Annunziatella, M., et al. 2023b, *ApJL*, 946, L16, doi: [10.3847/2041-8213/acb3a5](https://doi.org/10.3847/2041-8213/acb3a5)
- Pérez-González, P. G., Barro, G., Rieke, G. H., et al. 2024, arXiv e-prints, arXiv:2401.08782, doi: [10.48550/arXiv.2401.08782](https://doi.org/10.48550/arXiv.2401.08782)
- Polletta, M. d. C., Wilkes, B. J., Siana, B., et al. 2006, *ApJ*, 642, 673, doi: [10.1086/500821](https://doi.org/10.1086/500821)
- Rinaldi, P., Pérez-González, P. G., Rieke, G. H., et al. 2025, arXiv e-prints, arXiv:2504.01852, doi: [10.48550/arXiv.2504.01852](https://doi.org/10.48550/arXiv.2504.01852)
- Roberts-Borsani, G., Treu, T., Shapley, A., et al. 2024, *ApJ*, 976, 193, doi: [10.3847/1538-4357/ad85d3](https://doi.org/10.3847/1538-4357/ad85d3)
- Ronayne, K., Papovich, C., Kirkpatrick, A., et al. 2025, arXiv e-prints, arXiv:2508.20177, doi: [10.48550/arXiv.2508.20177](https://doi.org/10.48550/arXiv.2508.20177)
- Rusakov, V., Watson, D., Nikopoulos, G. P., et al. 2025, arXiv e-prints, arXiv:2503.16595, doi: [10.48550/arXiv.2503.16595](https://doi.org/10.48550/arXiv.2503.16595)
- Scholtz, J., Carniani, S., Parlanti, E., et al. 2025, arXiv e-prints, arXiv:2510.01034, doi: [10.48550/arXiv.2510.01034](https://doi.org/10.48550/arXiv.2510.01034)
- Setton, D. J., Greene, J. E., de Graaff, A., et al. 2024, arXiv e-prints, arXiv:2411.03424, doi: [10.48550/arXiv.2411.03424](https://doi.org/10.48550/arXiv.2411.03424)
- Setton, D. J., Greene, J. E., Spilker, J. S., et al. 2025, *ApJL*, 991, L10, doi: [10.3847/2041-8213/ade78b](https://doi.org/10.3847/2041-8213/ade78b)
- Taylor, A. J., Finkelstein, S. L., Kocevski, D. D., et al. 2024, arXiv e-prints, arXiv:2409.06772, doi: [10.48550/arXiv.2409.06772](https://doi.org/10.48550/arXiv.2409.06772)
- Taylor, A. J., Kokorev, V., Kocevski, D. D., et al. 2025, arXiv e-prints, arXiv:2505.04609, doi: [10.48550/arXiv.2505.04609](https://doi.org/10.48550/arXiv.2505.04609)
- Torralba, A., Matthee, J., Pezzulli, G., et al. 2025, arXiv e-prints, arXiv:2510.00103, doi: [10.48550/arXiv.2510.00103](https://doi.org/10.48550/arXiv.2510.00103)
- Trump, J. R., Arrabal Haro, P., Simons, R. C., et al. 2023, *ApJ*, 945, 35, doi: [10.3847/1538-4357/acba8a](https://doi.org/10.3847/1538-4357/acba8a)
- Umeda, H., Inayoshi, K., Harikane, Y., & Murase, K. 2025, arXiv e-prints, arXiv:2512.04208, doi: [10.48550/arXiv.2512.04208](https://doi.org/10.48550/arXiv.2512.04208)
- Valentino, F., Brammer, G., Gould, K. M. L., et al. 2023, *ApJ*, 947, 20, doi: [10.3847/1538-4357/acbefa](https://doi.org/10.3847/1538-4357/acbefa)
- Valentino, F., Heintz, K. E., Brammer, G., et al. 2025, *A&A*, 699, A358, doi: [10.1051/0004-6361/202553908](https://doi.org/10.1051/0004-6361/202553908)
- van der Walt, S., Colbert, S. C., & Varoquaux, G. 2011, *Computing in Science and Engineering*, 13, 22, doi: [10.1109/MCSE.2011.37](https://doi.org/10.1109/MCSE.2011.37)
- Wang, B., de Graaff, A., Davies, R. L., et al. 2024a, arXiv e-prints, arXiv:2403.02304, doi: [10.48550/arXiv.2403.02304](https://doi.org/10.48550/arXiv.2403.02304)
- Wang, B., Leja, J., de Graaff, A., et al. 2024b, *ApJL*, 969, L13, doi: [10.3847/2041-8213/ad55f7](https://doi.org/10.3847/2041-8213/ad55f7)
- Weibel, A., de Graaff, A., Setton, D. J., et al. 2024, arXiv e-prints, arXiv:2409.03829, doi: [10.48550/arXiv.2409.03829](https://doi.org/10.48550/arXiv.2409.03829)
- Williams, C. C., Tacchella, S., Maseda, M. V., et al. 2023, *ApJS*, 268, 64, doi: [10.3847/1538-4365/acf130](https://doi.org/10.3847/1538-4365/acf130)
- Williams, C. C., Alberts, S., Ji, Z., et al. 2024, *ApJ*, 968, 34, doi: [10.3847/1538-4357/ad3f17](https://doi.org/10.3847/1538-4357/ad3f17)
- Williams, R. J., Quadri, R. F., Franx, M., et al. 2010, *ApJ*, 713, 738, doi: [10.1088/0004-637X/713/2/738](https://doi.org/10.1088/0004-637X/713/2/738)
- Wuyts, S., Labbé, I., Franx, M., et al. 2007, *ApJ*, 655, 51, doi: [10.1086/509708](https://doi.org/10.1086/509708)
- Yan, Z., Inayoshi, K., Chen, K., & Guo, J. 2025, arXiv e-prints, arXiv:2512.11050, doi: [10.48550/arXiv.2512.11050](https://doi.org/10.48550/arXiv.2512.11050)
- Zhang, J., Egami, E., Sun, F., et al. 2025, arXiv e-prints, arXiv:2505.02895, doi: [10.48550/arXiv.2505.02895](https://doi.org/10.48550/arXiv.2505.02895)